EXPERIMENTALLY INFUSED ACTIVE SYSTEM OPTIMIZATION - THEORETICAL FRAMEWORK AND AIRBORNE WIND ENERGY CASE STUDY

by

Nihar Deodhar

A dissertation submitted to the faculty of
The University of North Carolina at Charlotte
in partial fulfillment of the requirements
for the degree of Doctor of Philosophy in
Mechanical Engineering

Charlotte

2018

Approved by:

_____
Dr. Christopher Vermillion

_____
Dr. Scott Kelly

_____
Dr. Peter Tkacik

_____
Dr. Yogendra Kakad

_____
Dr. Tao Hong

ABSTRACT

NIHAR DEODHAR. Experimentally Infused Active System Optimization - Theoretical Framework and Airborne Wind Energy Case Study. (Under the direction of DR. CHRISTOPHER VERMILLION)

This research pioneers formal combined plant and controller optimization (termed "co-design") schemes for complex systems where accurate but expensive experiments are fused with cheap but less accurate numerical simulations. This fusion of experiments with numerical modeling tools, referred to as experimentally infused optimization, addresses several challenges faced in co-design research. These challenges include strong coupling between the controller and plant, significant modeling uncertainties (which require the use of experiments), and high experimental costs. This research presents two unique iterative experimentally infused optimization approaches: One approach uses small "batches" of experiments at each iteration to identify the gradient of a performance index, whereas the other approach leverages tools from optimal design of experiments and hypothesis testing to efficiently explore and reduce the design space at each iteration. Both approaches incorporate a model correction term that improves the numerical model prediction after each set of experiments. For the latter approach, an original theoretical convergence bound on the numerical model improvement in the presence of noise-influenced experiments is presented and derived in this dissertation. Furthermore, both approaches have been validated for performance-critical parameters on a lab-scale airborne wind energy (AWE) system test platform at UNC Charlotte. Dimensional analysis has been used to show that this unique lab-scale platform produces results that replicate the full-scale flight behavior under uniformly-scaled system time constants. Overall, the quality of flight for the AWE

system is greatly improved using experimental infusion as compared to a pure numerical optimization approach.

ACKNOWLEDGMENTS

First of all, I would like to thank my advisor, Dr. Chris Vermillion, who has been a phenomenal mentor throughout my Ph.D. I largely credit him for my professional and personal development over the past few years. I would like to thank my committee members, Dr. Kelly, Dr. Tkacik, and Dr. Kakad, for assisting me through the academic process.

I would like to extend my appreciation toward all of the colleagues in my lab and the faculty members who participated in this research, both at UNC Charlotte and elsewhere. Furthermore, I would like to specifically thank Mr. and Mrs. Longbrook for all the Thanksgiving dinners. They made me feel at home even when I was far from home.

Finally, I thank my parents for the motivation and all of their sacrifices made in providing me with this wonderful opportunity.

TABLE OF CONTENTS

LIST OF FIGURES

LIST OF TABLES

CHAPTER 1: INTRODUCTION

A growing number of engineered systems rely both on robust physical designs and efficient control schemes. To optimize these "smart" systems, several researchers have developed combined plant and controller design techniques. This process is commonly known as *co-design*. In performing co-design on highly complex systems, heavy reliance on numerical simulations often results in sub-optimal solutions since numerical models of these complex systems are often inaccurate. On the other hand, heavy reliance on experimental characterization imposes time and cost challenges. Therefore, it is desirable to use a combination of accurate experiments and cheap numerical modeling techniques to efficiently optimize the plant and controller for complex systems. This research develops and validate formal techniques for fusing experiments with numerical modeling tools in the co-design process.

1.1 Background - Combined plant and controller optimization

A *plant* is defined as the set of physical components and processes in an active system that must carry out a prescribed task. A *controller* can be defined as the component that actively makes decisions and manipulates variables in real-time to achieve that task. Several strategies have been proposed in the literature to optimize the plant parameters ($\mathbf{p_p}$) and controller parameters ($\mathbf{p_c}$). The most popular types of co-design techniques include iterative, sequential, nested and simultaneous approaches (see Figure 1, [1]). The iterative

strategy optimizes the plant and controller alternately until a convergence criterion is satisfied. The sequential approach is a specific case of iterative optimization with one iteration of the plant followed by one iteration of the controller. The nested strategy deploys an inner loop/outer loop type of framework in which the controller is optimized in its entirety (in the inner loop) after every iteration of the plant optimization (in the outer loop). Lastly, the simultaneous optimization strategy considers all the parameters during every iteration without distinguishing between the plant and controller parameters. The performance of the iterative and sequential strategies is heavily influenced by the level of coupling between the plant and controller parameters. Such coupling arises when the optimal control design depends on the plant and vice versa. Co-design in the presence of coupling has been highlighted through a diverse range of applications in the literature. For instance, a structural system is studied in [2], micro-electrical mechanical systems are examined in [3], two-link robotic manipulators are studied in [4] and [5], and [6] and [7] apply co-design to an automotive suspension system. A similar plant-controller coupling is highlighted in [1] using an electric motor application. The iterative and sequential approaches may fail in the presence of a coupling between the plant and controller parameters, as shown by [8] and [9]. To address the challenges arising due to coupled dynamics, [10] and [11] use a decomposition-based method to solve the co-design problem, whereas [12] incorporates the process of sequential optimization using direct transcription for an active suspension system. A different approach for combined plant and controller parameters, leveraging a control proxy function, is detailed in the work of [13], [14], and [15]. There, the plant objective function is independent of control parameters, and the controller objective depends only on the optimal plant. The control proxy function modeled as a function of plant pa-

rameters is used, along with the original objective function, for optimization. This approach mitigates the shortcomings in a typical iterative optimization but only considers unidirectional coupling, thereby leaving the controller constraints dependent on plant parameters. Under a variety of conditions, the simultaneous approach guarantees convergence under coupled plant and controller dynamics (see [8] and [9]). However, simultaneous optimization is computationally burdensome. A nested strategy, on the other hand, has proven to be more efficient than simultaneous strategies, and has been adopted in several applications. For instance, [16] and [17] use a nested loop approach to optimize the suspension system for a quarter car model. [18] applies the nested approach to the optimization of an elevator system.

While the aforementioned numerical techniques have made great strides in terms of computational efficiency and convergence guarantees, their efficacy primarily depends on an accurate plant model. When the plant model ceases to be accurate, even the best numerical optimization can yield plant and control parameters that are far from the true optimum.

In an attempt to address the limitations of purely numerical optimization, the authors of [19] carried out initial studies wherein experimental data was used to guide the plant and controller toward their true optima. The plant was physically modified at each iteration, and controller gains were adjusted based on an experimentally-identified Jacobian matrix. Similarly, [20] emphasizes the need for experimental co-design but ends up using simulations instead. [21], on the other hand, uses experimental optimization for a similar robot manipulator as in [19]. However, both [19] and [21] rely on pure experimental results to carry out the optimization. Relying solely on experiments to optimize a system design can be problematic, however, when these experiments are costly in terms of time and money.

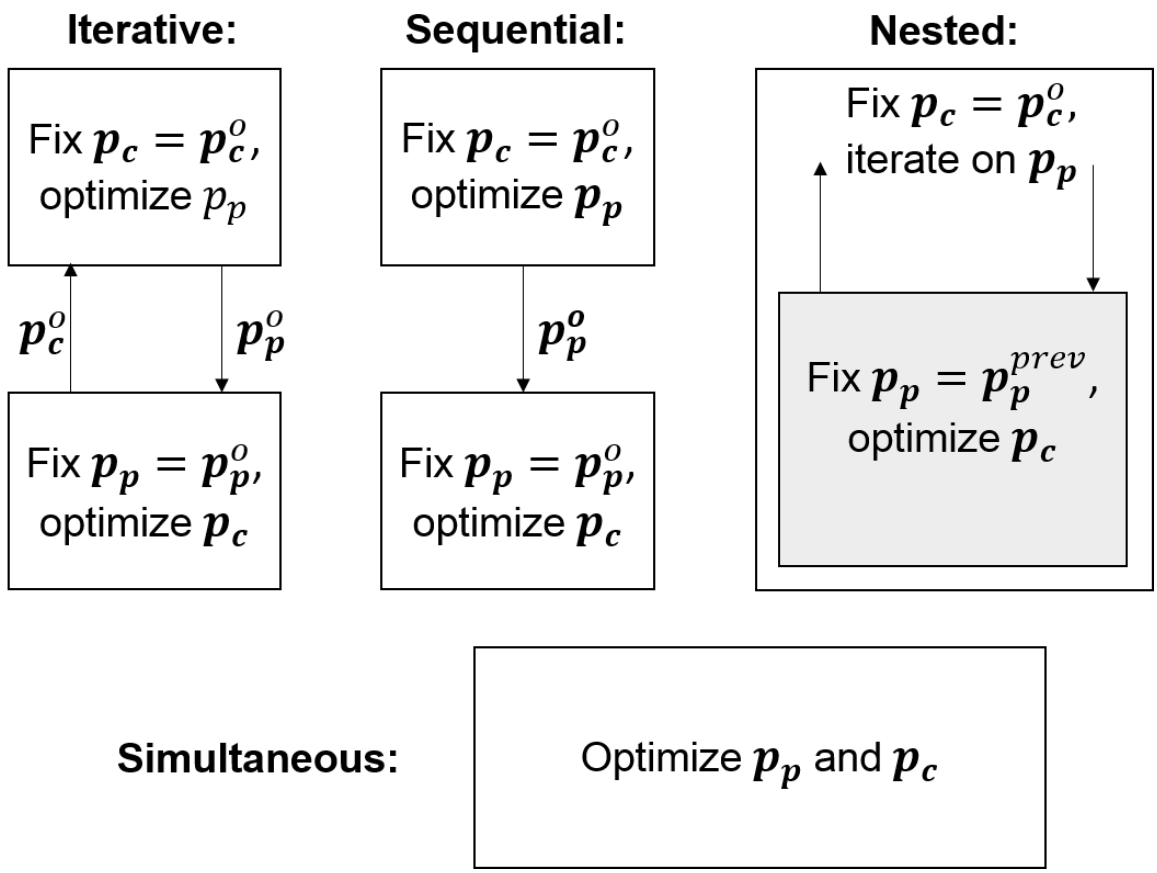

Figure 1: Different approaches used in combined plant and controller optimization. $\mathbf{p_p}$ and $\mathbf{p_c}$ denote plant and controller parameters respectively. $\mathbf{p_p}^0$ and $\mathbf{p_c}^0$ represent the initial conditions for optimization [1].

Thus, for systems where an imperfect numerical model exists, a better approach is to fuse small numbers of accurate but expensive experiments with larger numbers of less accurate but cheap numerical simulations. This fusion of experiments with numerical modeling tools is precisely the focus of this research.

1.2 Airborne wind energy (AWE) systems - case study application

AWE systems replace traditional tower-mounted wind turbines with flexible tethers and a lifting body. This design enables the AWE systems to harness strong, consistent winds at high altitudes (up to 600 m), as described in [22]. Altaeros Energies [23], Ampyx Power

[24], Google-owned (X) Makani Power [25], Enerkite [26], Kitegen [27], and Windlift [28] are some of the active companies in the field of AWE. Ampyx, Windlift, and Makani use a rigid wing design with control surfaces. Enerkite and Kitegen incorporate the use of kite-like lifting bodies to fly crosswind patterns. Altaeros Energies, on the other hand, uses a lighter-than-air-system in the form of an annular aerostat (Figure 2) that houses the turbine.

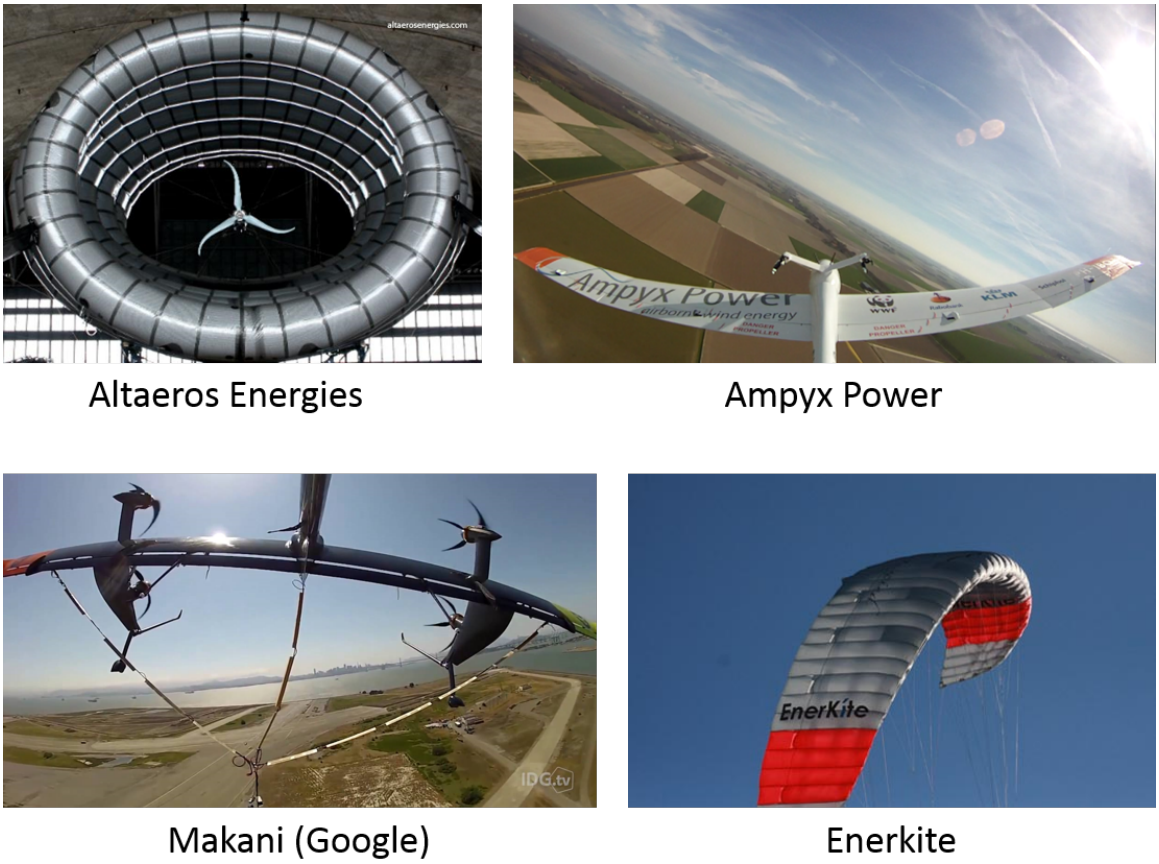

Figure 2: The prototypes used by a few active airborne wind energy system manufacturers. Sources: [23], [24], [25] and [26].

AWE systems fall under the category of systems with complex dynamics and imperfect numerical models. Moreover, the plant and controller dynamics are coupled in the case of AWE systems. One instance where this can be seen involves the center of mass location (plant parameter) and the pitch angle set point (controller parameter). The optimal center

of mass location depends on the pitch angle set point, and vice versa. In such instances of plant and controller coupling, it is desired to use appropriate co-design techniques to optimize the AWE system parameters.

Although several numerical optimization techniques have been explored for different types of AWE systems, the majority of them do not address coupling issues. Moreover, all of the aforementioned references have placed great emphasis on the use of simulations. For instance, [29] characterizes crosswind flight for kite systems while relying on imperfect numerical models. More recently, co-design techniques were applied in the field of AWE systems, specifically in [30] and [31], where a numerical optimization was carried out for crosswind flight using the nested approach. Similarly, the work by the authors of [32] also exploits a local, simulation-based approach for co-design of an AWE system.

AWE systems, however, demonstrate several complex phenomena such as unsteady flow effects due to vortex shedding, added mass effects, complex catenary tether shapes, and so on. These phenomena present significant challenges to the development of accurate models. As a result, existing numerical models and the optimizations based on those numerical models are far from perfect. [33] and [34] are some of the few contributors in the field of full-scale testing of AWE systems. In particular, the flight characterization of a lighter-than-air type of AWE systems was achieved in [33] and [34]. While these experiments provide a much better understanding of the system than numerical simulations, they are not cost-effective. Due to the aforementioned full-scale testing costs, it is highly beneficial to devise a lab-scale test environment wherein it is possible to iterate quickly and inexpensively between multiple lifting body and controller designs. In order to study the open-loop characteristics of such systems economically, the authors of [35] developed a small-scale

test setup. A similar experimental framework has been used in [36] and [37] to characterize AWE systems under closed-loop control.

All of the aforementioned work on AWE systems is either purely numerical or purely experimental. The numerical techniques fail to converge upon a true optimum in the presence of modeling uncertainties, whereas purely experimental optimization is extremely time-consuming and does not leverage existing numerical models, imperfect as they may be. For these reasons, AWE represents an ideal application for studying the experimentally infused optimization tools described in this research.

1.3 Problem statement and research contributions

Due to the aforementioned co-design challenges (in particular, the coupled dynamics and unmodeled effects) faced in a wide array of complex systems, including AWE systems, it is extremely desirable to develop a framework that fuses the cost-effective numerical models with accurate and optimally designed experiments. In considering suitable iterative design optimization frameworks that fuse experiments with numerical simulations, the following three questions can be posed:

- Question 1: How should experimental and simulation points be determined at each iteration to maximize the information learned?
- Question 2: How can the numerical model be improved at every iteration, based on experimental results, in order to globally converge to the optimal design parameters?
- Question 3: How many iterations are needed to converge to the optimal design in the case of disturbances and experimental noise?

This research examines two frameworks for formally addressing the challenge of optimally fusing experiments with numerical models. The first framework, illustrated conceptually in Figure 3 and detailed in Chapter 3, involves several steps that are carried out iteratively:

- Generate experiments within the *local* parameter space surrounding the estimated optimal design based on the numerical system model.
- Run those experiments.
- Compute a correction to the numerical model based on the experiments.
- Run a full numerical optimization with the corrected model, then repeat the process.

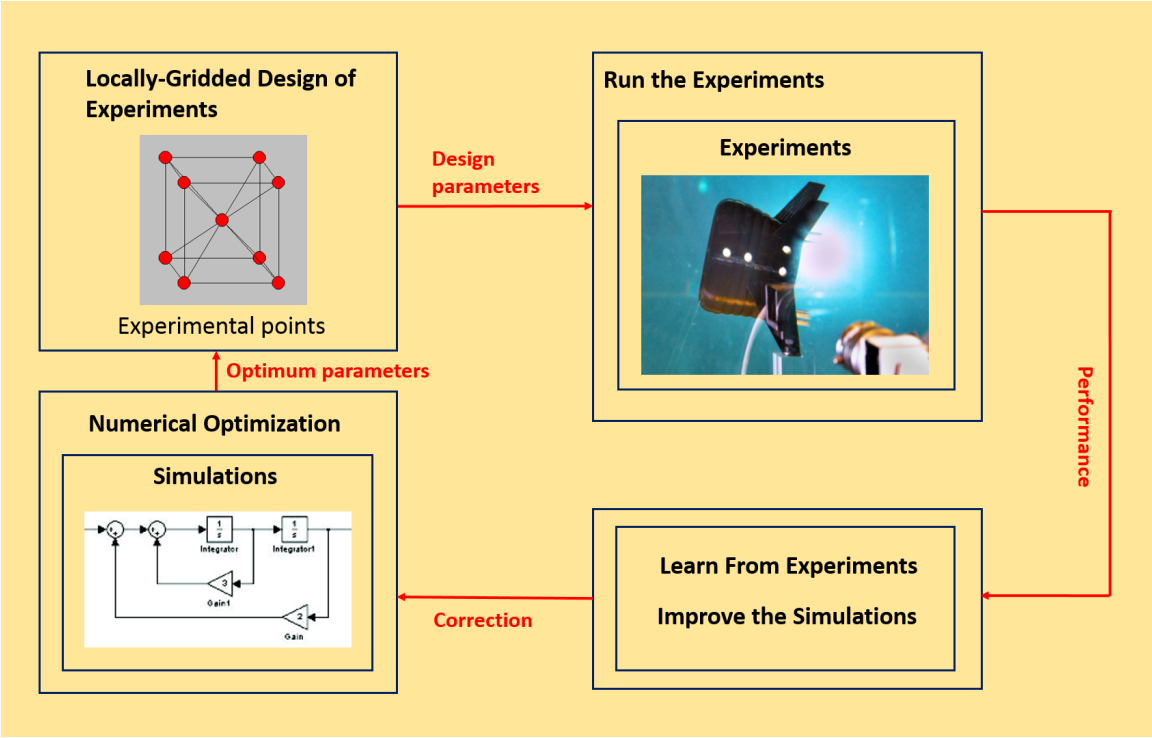

Figure 3: General steps involved in experimentally infused plant and controller optimization with small "batches" of local experiments at each iteration (see Chapter 3 for details).

This process addresses numerical modeling inaccuracies but may not lead to a global optimum due to a locally-gridded experimental design space.

A second *global* framework is described conceptually in Figure 4 and then detailed in Chapter 5:

- Perform an optimal design of experiments (DoE) and numerical simulations that spans a prescribed design space.
- Run the experiments and simulations.
- Fit a response surface to the data obtained from simulations and experiments.
- Improve the numerical model at each iteration based on the results of all previous experiments.
- Reduce the feasible design space for subsequent iterations.

The aforementioned framework addresses the first two questions posed earlier. A solution to the third question is presented in Chapter 6. In summary, the contributions of this research are as follows:

- Designing an iterative co-design framework to fuse experiments with numerical simulations using gradient-based DoE;
- Globalizing the iterative framework using optimal DoE, response characterization, and statistical hypothesis testing tools;
- Deriving a bound on the convergence of the improved numerical model to the true system;

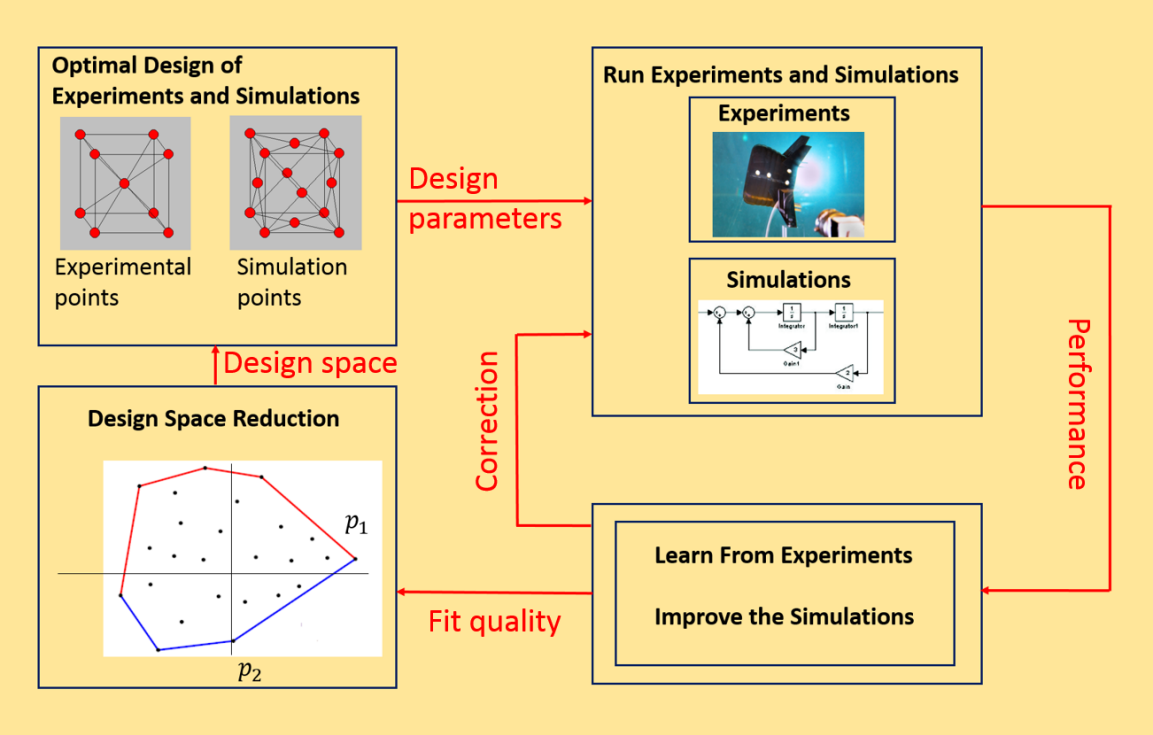

Figure 4: Flowchart summarizing the necessary steps for a successfully fused numerical/experimental optimization with global optimal DoE techniques used at each iteration (see Chapter 5).

- Establishment of dynamic equivalence between the full-scale and lab-scale test framework for a lighter-than-air AWE system;

- Experimentally validating the gradient-based DoE for two AWE design parameters, using the lab-scale setup;

- Experimentally validating the optimal DoE framework for two and four AWE design parameters, using the lab-scale setup.

CHAPTER 2: AWE SYSTEM - DYNAMIC MODEL AND LAB-SCALE EXPERIMENTAL SETUP

This work uses the Altaeros Buoyant Air Turbine (BAT) as a case study. The Altaeros BAT is a lighter-than-air AWE system with a horizontal-axis turbine suspended within an annular shell. The system shown in Figure 5 is the full-scale prototype flown by Altaeros in 2012. The BAT consists of four main components, namely an annular shroud, a horizontal

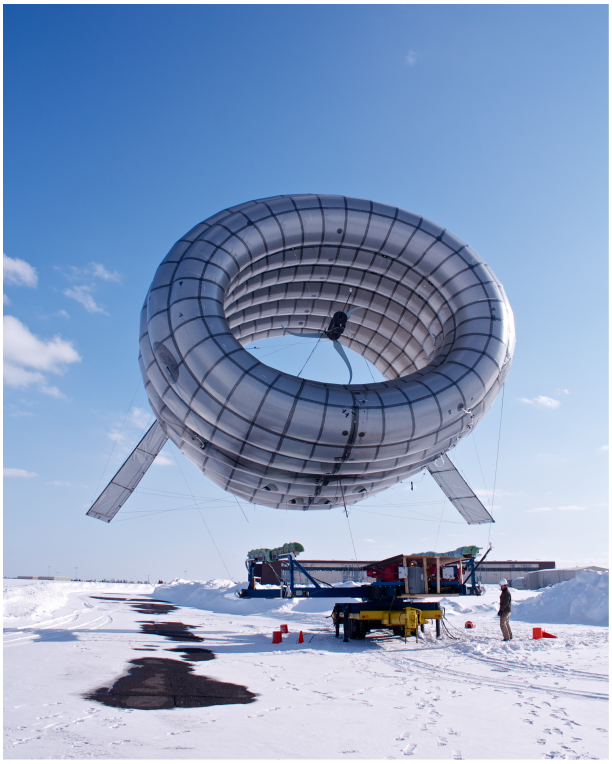

Figure 5: Full-scale prototype of Buoyant Airborne Turbine (BAT) during 2012 flight testing at Loring Air Force Base. (altaerosenergies.com)

axis turbine, three tethers, and a ground station.

- Annular shroud: The annular shroud geometry originates from NACA airfoil cross

sections, which are cambered upward on the lower and upper surfaces of the BAT to provide lift. The shroud is symmetric about the vertical plane; however, the side-walls themselves are designed with asymmetric airfoil cross sections. A ballonet is included to maintain desired pressure inside the shroud by regulating the supply of helium.

- Turbine: The 2012 Altaeros prototype was equipped with commercially-available Skystream 3.7 Turbine, with a rated power of 2.4 kW at a rated wind speed of 10 $\frac{m}{s}$. This turbine was used purely for demonstration purposes. The target output of a production system is approximately 100 kW. This can be achieved with a bigger shroud and a greater rated wind speed.

- Tethers: The most recent Altaeros BAT geometry features three tethers, two of which are made of high-performance Dyneema fiber, one of which is a structurally reinforced conductive cable. Each of the tethers has a $\frac{3}{8}$ inch (0.01 meter) diameter.

- Ground station: A rotating platform carrying the winches along with main flight controller and other drives forms the ground station. This mobile station is deployed at the desired location using a tow truck.

2.1 Dynamic model of the BAT

Key parameters used in deriving dynamic equations for the BAT are shown in Figure 6.

A simplified dynamic model of the BAT is introduced in [33] and [35]. However, the BAT exhibits several complex non-linear phenomena that are not sufficiently described using numerical models. These include added mass effects, unsteady flow effects, stall,

and complex tether dynamics.

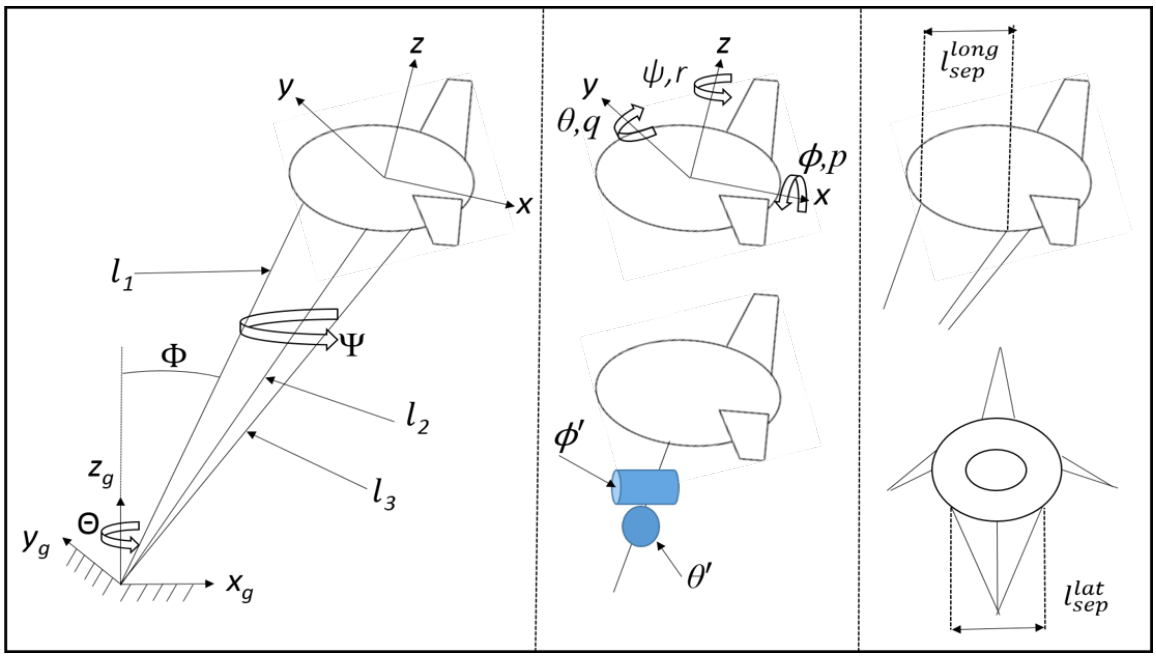

Figure 6: Illustration of the generalized coordinates (Φ, Θ, and Ψ) and key physical aspects which form the basis for the dynamic model.

In order to represent the multi-tether system dynamics through ordinary differential equations and model the tethers as simple kinematic links, the three tether configuration is approximated as a single main tether of length L_t with a controlled spherical bridle joint at the top. Ultimately, this results in a configuration where the position of the center of mass of the aerostat can be described based on Φ (zenith angle), Θ (azimuth angle), and L_t (average tether length), whereas the aerostat's orientation requires the generalized coordinates associated with the spherical bridle joint, namely Ψ, an *uncontrolled* twist angle, θ', a controlled "induced-pitch" angle (induced through asymmetric length adjustment of the forward and aft tethers), and ϕ', a controlled "induced-roll" angle (induced through the asymmetric length adjustment of the port and starboard tethers). The aforementioned

induced angles, $\phi^{'}$ and θ' are related to the tether lengths by:

$$\phi' = tan^{-1}(\frac{l_3 - l_2}{l_{sep}^{lat}}) \tag{1}$$

$$\theta' = tan^{-1}(\frac{l_1 - 0.5(l_2 + l_3)}{l_{sep}^{long}}) \tag{2}$$

where l_{sep}^{long} and l_{sep}^{lat} are longitudinal and lateral tether attachment separation distances, respectively. The control inputs are the tether release speeds, $\bar{u}_i$, which are given by:

$$\bar{u}_i = \frac{d}{dt} l_i \tag{3}$$

Here, ϕ' and θ' are introduced in order to model the three tethered system as a single kinematic link of length L_t, plus two rotational degrees of freedom (ϕ' and θ') that characterize the *differences* in tether lengths. Modeling the multi-tether system in this way results in a set of ordinary differential equations (ODEs), rather than the set of differential algebraic equations (DAEs) that would result from modeling each tether as its own kinematic constraint. The system dynamics, as derived using an Euler-Lagrange approach, are given by:

$$D(Q)\ddot{Q} + C(Q,\dot{Q})\dot{Q} + g(Q) = \tau(Q,\dot{Q},V_{wind},\psi_{wind}) \tag{4}$$

$$X = f(Q,\dot{Q}) \tag{5}$$

$$\Omega = g(Q,\dot{Q}) \tag{6}$$

where:

$$Q = [\Phi \;\; \Theta \;\; \Psi \;\; L_t \;\; \theta' \;\; \phi'] \tag{7}$$

$$X = [x \;\; y \;\; z \;\; u \;\; v \;\; w] \tag{8}$$

$$\Omega = [\phi \;\; \theta \;\; \psi \;\; p \;\; q \;\; r] \tag{9}$$

Here, V is the flow speed, and ψ_{flow} and τ represent the flow direction and vector of generalized forces and moments. The generalized forces and moments are functions of α (angle of attack) and β (side slip angle), which describe the orientation of the apparent wind velocity vector with respect to body-fixed coordinates. The variables in equations (8) and (9) are functions of the generalized coordinates in equation (7) and represent the translational and rotational dynamics, respectively.

2.2 Water channel setup at UNC Charlotte

Initial work by one of the authors in [34] and [35] provides a description of a lab-scale testing framework that uses a water channel and 3D printed models to characterize the passive flight dynamics of a $1/100^{th}$-scale aerostat for a lighter-than-air wind energy system. The use of a lab-scale water channel setup significantly reduces cost and testing time when compared to the full-scale system. In order to conduct cost-effective experiments, this research utilizes the water channel test setup at UNC Charlotte, which is shown in Figure 7. The UNC Charlotte water channel is the 5^{th} largest in the U.S., with a 1 meter $\times$ 1 meter cross section and flow speeds up to 1 $\mathrm{m/s}$. This platform enables rapid and inexpensive iteration through new plant and control system designs. This setup consists of the following major components:

- Three DC motors mounted on a frame located at the top of the channel in Fig. 7. The motors are attached to individual tethers, thereby controlling individual tether release rates.

- Three high-speed cameras for image acquisition, each capable of a frame rate of

340 frames/sec. Two cameras are positioned on the side of the water channel (one directly perpendicular and the other downstream, at an angle of 45 degrees), and one is positioned at the bottom of the channel (looking upward, perpendicular to the channel).

- A high speed (6 core, 64 GB) target computer that carries out real-time image processing and feedback control at a sample time of 0.025 s. The target application performs image processing, geometric transformations to resolve the position and orientation of the BAT and executes the control algorithm.

- A host computer that acts as a link between the target PC and the operator. The host computer operates a graphic user interface (GUI) to command rapid controller changes onto the target PC and renders the real-time plots.

- A $1/100^{th}$-scale, 3D printed model of the tethered lifting body that is flown in the test section of the water channel. Rapid reconfigurability of the model is made possible through several design features that are illustrated in Figure 8. These include ballast holes for varying the center of mass and moments of inertia, variable tether attachment points, and a drag screen slit that accommodates a mesh screen that replicates the drag associated with a spinning rotor.

2.3 Real-time control and controller structure

The controller is designed to track three different set points, namely altitude (z_{sp}), pitch (θ_{sp}) and roll (ϕ_{sp}). Tracking is achieved by using tether release speeds as the control inputs to three independent motors for the port, the starboard, and the central tether. Figure

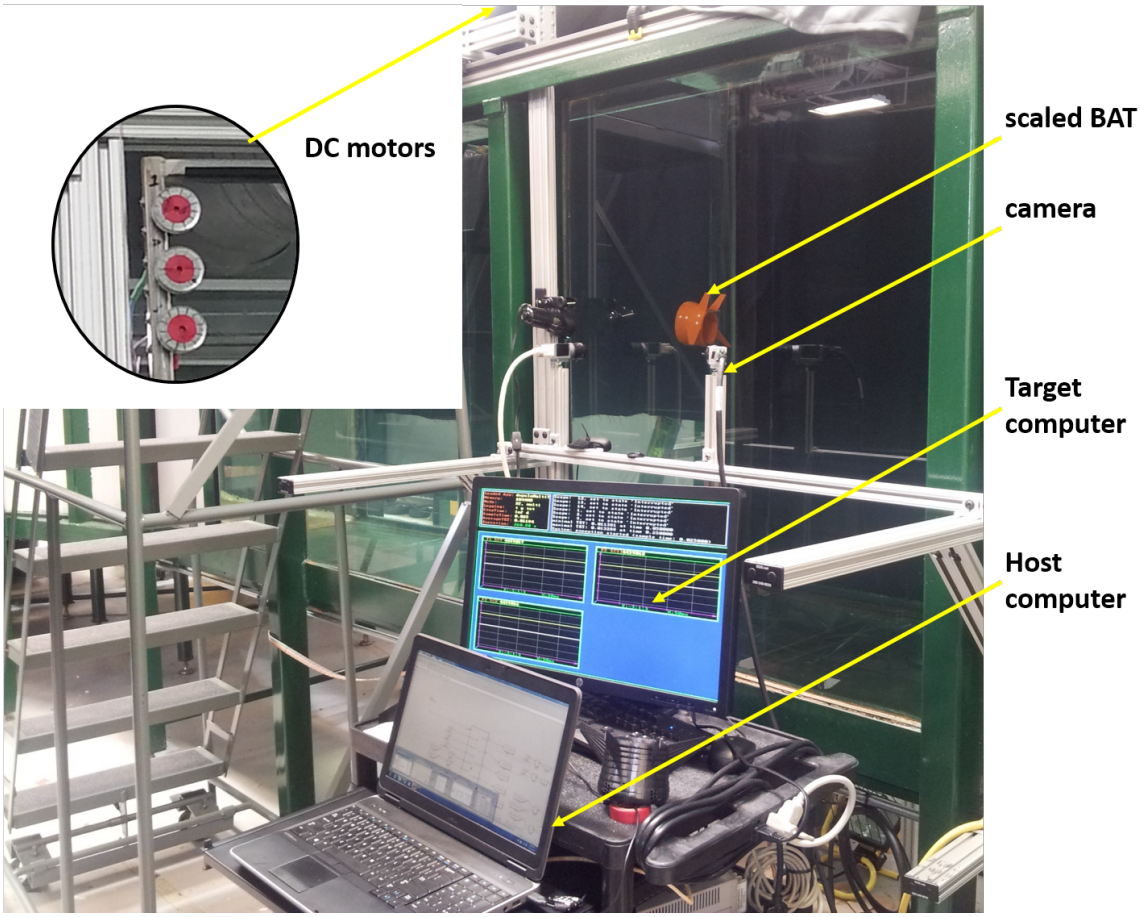

Figure 7: Water channel test framework at UNC-Charlotte.

9 shows a block diagram of the controller. The average tether release speed ($\bar{v}_z$), difference between central/peripheral tether release speeds ($\bar{v}_\theta$), and port/starboard tether release speeds ($\bar{v}_\phi$) are related to the tracking errors in altitude (z_e), pitch (θ_e) and roll (ϕ_e) by the transfer functions $G_z(s)$, $G_\theta(s)$ and $G_\phi(s)$ respectively. These transfer functions, which reflect filtered PD controllers, are given by the following expressions:

$$G_z(s) = \frac{k_d^z s + k_p^z}{\tau_z s + 1}, \tag{10}$$

$$G_\theta(s) = \frac{k_d^\theta s + k_p^\theta}{\tau_\theta s + 1}, \tag{11}$$

$$G_\phi(s) = \frac{k_d^\phi s + k_p^\phi}{\tau_\phi s + 1}. \tag{12}$$

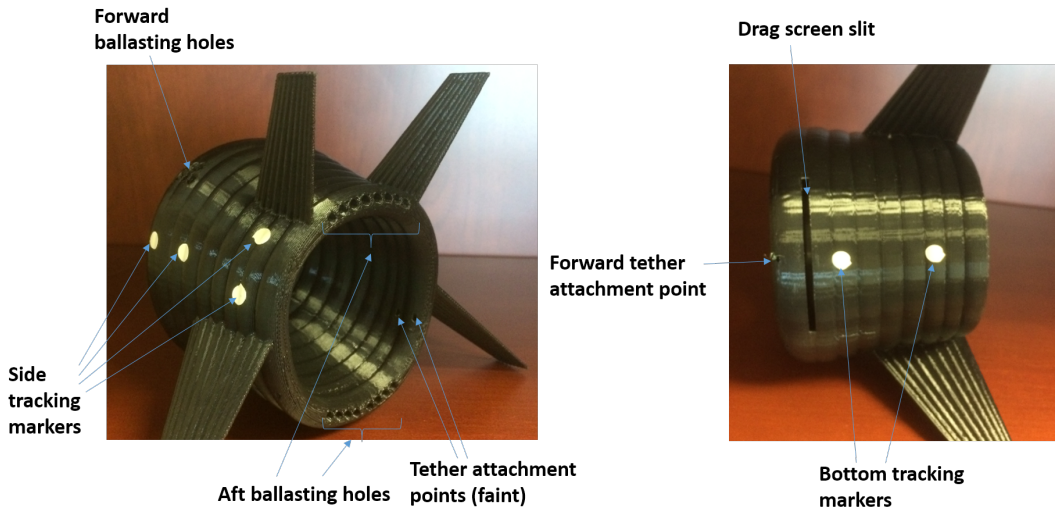

Figure 8: Isometric view and bottom view of a 1/100-scale BAT model, illustrating the ability for rapid reconfiguration between test runs.

Integral control is not necessary for steady-state tracking in this application, due to pure integrators in the plant dynamics. Since the goal is to attain a stable configuration, ϕ_{sp} is always desired to be zero. The tether release speeds, $\bar{u}_{center}$, $\bar{u}_{stbd}$ and $\bar{u}_{port}$, serve as control inputs to three motors and are related to $\bar{v}_z$, $\bar{v}_\theta$ and $\bar{v}_\phi$ as follows:

$$\mathbf{u} = A\mathbf{v} \tag{13}$$

$$A = \begin{bmatrix} 1 & -1 & 0 \\ 1 & 1 & 1 \\ 1 & 1 & -1 \end{bmatrix} \tag{14}$$

where the n^{th} column of A relates $\mathbf{v}$ to the individual motor commands, $\mathbf{u}$, where $\mathbf{v} = [\bar{v}_z\ \bar{v}_\theta\ \bar{v}_\phi]^T$ and $\mathbf{u} = [\bar{u}_{center}\ \bar{u}_{stbd}\ \bar{u}_{port}]^T$.

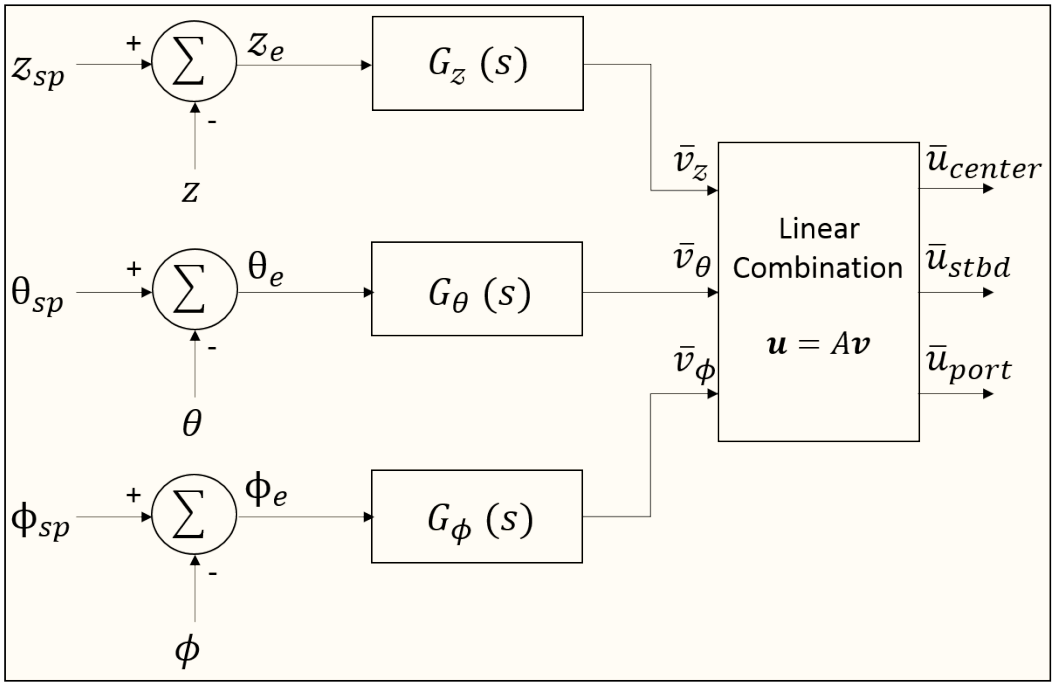

Figure 9: Block diagram of the controller to track altitude and attitude set-points during flight [37]. Altitude set point was chosen within practical constraints.

2.4 Dynamic equivalence analysis between the full-scale and lab-scale system

In order to fully replicate the behavior of the full-scale system using a lab-scale setup, the plant, controller and the operating parameters should be scaled precisely. In order to determine the required scaling, formal dimensional analysis tools were utilized in this research.

In fact, a few studies have already applied dimensional analysis to small-scale testing of tethered systems. Specifically, the authors of [38] and [39] establish the dynamic equivalence of a multi-tethered aerostat for a radio telescope at $1/3^{rd}$ scale. Although the authors sacrifice precise accuracy of Reynolds number matching in this case, the Reynolds numbers for that application are large enough that aerodynamic coefficients are insensitive to

Reynolds number. A dimensional analysis for single-tethered systems is presented in [40] and [41]. However, this dimensional analysis does not consider density and buoyancy properties that are equally important to lighter-than-air systems such as the Altaeros BAT. The dynamic equivalence tools developed in this research focus on the Altaeros BAT as a case study. However, the lab-scale platform is more generally applicable to a wide range of tethered systems with rigid lifting bodies.

The goal is to derive a set of dimensionless variables that provide specific guidance as to how the model and experimental parameters need to be chosen in the lab-scale, water channel environment in order to produce dynamically-equivalent behavior to the full-scale system. To do this, a Buckingham Pi-based dimensional analysis is used for the dynamic model and the controller. The first step in Buckingham Pi-based dimensional analysis is to derive a set of variables (and corresponding dimensions) that are sufficient to fully characterize the dynamics. From this set of variables and dimensions, it is possible to derive a set of dimensionless variables that should be matched at both scales.

2.4.1 Dimensional analysis for plant parameters

Because the variables in equations (8) and (9) are directly *dependent* on the variables in equation (7), only the variables in equation (7) need to be considered in the subsequent dimensional analysis. In order to arrive at a minimal set of variables, the following assumptions are made:

- Mass distribution is identical at lab-scale and full-scale, which renders the moments of inertia static functions of the mass and geometric properties. This assumption is satisfied through design and proper ballasting of 3D printed models.

- Aerodynamic coefficients are independent of the Reynolds number within the Reynolds number ranges seen in the water channel (75,000 at a 1 $\frac{m}{s}$ flow speed, using chord length as the reference length) and full-scale system (5,000,000 at a 10 $\frac{m}{s}$ wind speed). Hence, the viscosity of the medium is neglected as a physical dependency. The validity of this assumption is further assessed through force and moment characterization in [42]. Table 1 lists the remaining relevant variables and corresponding units.

Table 1: Physical dependencies used to describe the characteristics of the lifting body.

No.	Parameters	Units
1	L_t	m
2	L_c	m
3	d_t	m
4	M_a	kg
5	ρ	$kg \cdot m^{-3}$
6	V	$m \cdot s^{-1}$
7	g	$m \cdot s^{-2}$
8	$\dot{\Theta}$	s^{-1}
9	$\ddot{\Theta}$	s^{-2}
10	$\dot{\Phi}$	s^{-1}
11	$\ddot{\Phi}$	s^{-2}
12	$\dot{\Psi}$	s^{-1}
13	$\ddot{\Psi}$	s^{-2}
14	λ	$kg \cdot m^{-1}$

Buckingham Pi-based dimensional analysis results in the following dimensionless groups:

$$\Pi_{plant} = \left\{ \frac{L_c}{L_t}, \frac{L_t}{d_t}, \frac{L_t^3 \rho}{M_a}, \frac{\lambda L_t}{M_a}, \frac{g L_t}{V^2}, \frac{L_t \dot{\Theta}}{V}, \frac{L_t^2 \ddot{\Theta}}{V^2}, \frac{L_t \dot{\Phi}}{V}, \frac{L_t^2 \ddot{\Phi}}{V^2}, \frac{L_t \dot{\Psi}}{V}, \frac{L_t^2 \ddot{\Psi}}{V^2} \right\} \tag{15}$$

Interpretation of dimensional analysis results

The first two terms in (15) demonstrate that geometric similarity must be preserved between the lab-scale and full-scale models in order to achieve equivalent dynamic performance; thus, all linear dimensions (including the length, width, and height of the aerostat, as well as the tether length) must scale by the same amount. This overall scale factor, X_s is given by:

$$X_s = \frac{L_c^{labscale}}{L_c^{fullscale}}. \tag{16}$$

The third and the fourth dimensionless terms reflect the need to preserve net buoyancy between scales. The fifth term is equivalent to the *Richardson number* or $(1/Froude\ number^2)$. It requires the velocity to be scaled proportionally to the square root of length. Based on the first through fifth dimensionless terms, the following guidelines for achieving dynamic equivalence may be discerned:

- Scale L_t, L_c, and d_t to maintain geometric similarity.
- Scale M_a to maintain net buoyancy.
- Scale λ to preserve the ratio of tether mass to lifting body mass.
- Scale V such that $V \propto \sqrt{X_s}$.

Physically, the aforementioned scaling guidelines are satisfied in the following ways:

- The models are flown close to the maximum possible altitude attainable in the water channel in order to emulate high-altitude flight. For a 1/100-scale model, a flight altitude of 80cm emulates full-scale flight at 80m.

- The models are 3D printed out of low-density ABS plastic, which results in a specific gravity of approximately 0.5. Lead wires are used to increase the density of the models to maintain net buoyancy, while also moving the center of mass to the desired location.

- The tethers are ballasted with an appropriate number of sinkers to preserve the ratio of tether mass to lifting body mass. Because dynamic performance has not always been found to be sensitive to λ, the tethers are not ballasted in every test instance.

- The UNC-Charlotte water channel provides flow speeds up to 1 $\frac{m}{s}$, thereby emulating wind speeds up to 10 $\frac{m}{s}$ on the full-scale system.

The aforementioned scaling guidelines are based on the first five dimensionless variables of equation (15). However, in the succeeding dimensionless parameters, there is a direct variation of the velocity and length scales, thus rendering it impossible to follow the aforementioned scaling laws *and* achieve dynamic equivalence according to the sixth through eleventh dimensionless variables in equation (15). This contradiction can be resolved by introducing a normalized time, $\bar{t} = at$, which is reflective of uniformly scaled time constants (altered through the "stretching" factor, a) at small-scale versus full-scale.

A new set of dimensionless groups can be derived in scaled time as follows:

$$\Pi_{plant} = \left\{ \frac{L_c}{L_t}, \frac{L_t}{d_t}, \frac{L_t^3 \rho}{M_a}, \frac{\lambda L_t}{M_a}, \frac{\bar{g} L_t}{\bar{V}^2}, \frac{L_t \frac{d\Theta}{d\bar{t}}}{\bar{V}}, \frac{L_t^2 \frac{d^2\Theta}{d\bar{t}^2}}{\bar{V}^2}, \frac{L_t \frac{d\Phi}{d\bar{t}}}{\bar{V}}, \frac{L_t^2 \frac{d^2\Phi}{d\bar{t}^2}}{\bar{V}^2}, \frac{L_t \frac{d\Psi}{d\bar{t}}}{\bar{V}}, \frac{L_t^2 \frac{d^2\Psi}{d\bar{t}^2}}{\bar{V}^2}, a \right\} \quad (17)$$

where $\bar{V}$ and $\bar{g}$ represent flow speed and gravitational acceleration in scaled time. Examination of the dimensionless groups in (17) reveals that dynamic similarity can be obtained

by scaling time as a function of the square root of the length scale, i.e.,

$$a = \frac{\bar{t}}{t} \propto \frac{1}{\sqrt{X_s}}. \tag{18}$$

It follows that $\bar{V} \propto L_t$ and $\bar{g} \propto L_t$, from which we can see that all of the dimensionless parameters of (17) are matched at lab- and full-scale, with the exception of a, the time scale. Thus, by taking appropriate measures to match the first five dimensionless parameters at both lab-scale and full-scale, the remaining six dimensionless parameters are *automatically* matched. *It therefore follows from this analysis that under appropriate scaling of design parameters, as indicated above, the full-scale dynamic behavior can be replicated at lab-scale with the only difference being uniformly scaled time constants.*

2.4.2 Dimensional analysis for controller parameters

In order to correlate controller parameters in the water channel with full-scale flight control parameters, the dimensional analysis has been extended to include control parameters. The *additional* parameters introduced through the flight controller include:

k_p^z -= Proportional gain for altitude, $\frac{m/s}{m}$

k_d^z = Derivative gain for altitude, $\frac{m}{m}$

k_p^θ = Proportional gain for pitch angle, $\frac{m/s}{rad}$

k_d^θ = Derivative gain for pitch angle, $\frac{m}{rad}$

k_p^ϕ = Proportional gain for roll angle, $\frac{m/s}{rad}$

k_d^ϕ = Derivative gain for pitch angle, $\frac{m}{rad}$

$\tau_{z,\theta,\phi}$ = Filter time constant, s

Since k_d^z is already dimensionless, it can be removed from the analysis, and the resulting

analysis yields 8 dimensionless parameters:

$$\Pi_{controller} = \left\{ \frac{L_t}{k_d^\theta}, \frac{L_t}{k_d^\phi}, \bar{t}k_p^z, \frac{V}{k_p^\theta}, \frac{V}{k_p^\phi}, \frac{\bar{t}}{\tau_z}, \frac{\bar{t}}{\tau_\theta}, \frac{\bar{t}}{\tau_\phi} \right\} \tag{19}$$

Combining this set of dimensionless parameters with the earlier observation that $a \propto \sqrt{L_t}$ yields the following set of control parameter scaling laws:

$$\begin{aligned} k_d^\theta, k_d^\phi &\propto L_t \\ k_p^z &\propto \frac{1}{\sqrt{L_t}} \\ k_p^\theta, k_p^\phi &\propto \sqrt{L_t} \\ \tau_{z,\theta,\phi} &\propto \sqrt{L_t} \end{aligned}$$

2.4.3 Lab-scale validation of scaling laws

To validate the dimensional analysis at *lab-scale*, three different scale models (as shown in Figure 10) were tested in the water channel setup of Figure 7. L_c, L_t, M_a, and V were adjusted for each of the scaled model tests to preserve the non-dimensional variables of (17). Table 2 provides the exact values of these variables used in the validation tests. Each test was run in an open-loop mode (with control inputs equal to zero) using the parameters given by Table 2.

Table 2: Design and test parameters for the three models used in the scaling validation tests.

Variable (units)	Model 1	Model 2	Model 3
Scale factor X_s	0.0075	0.01	0.0125
Time scale a	11.54	10	8.94
L_c (cm)	5.625	7.5	9.375
L_t (cm)	45.7	61	76
M_a (g)	135	180	225
V (cm/s)	26	30	33.5

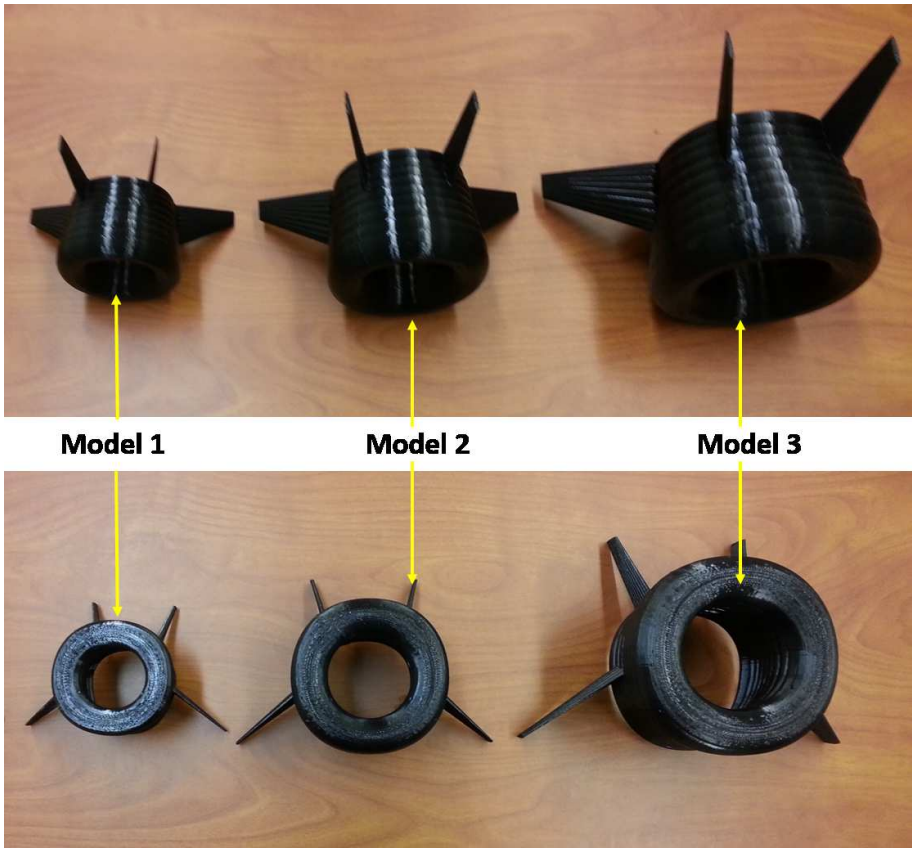

Figure 10: 3D printed lab-scale models of the BAT that were used in establishing dynamic similarity across different scales.

Figure 11 and Figure 12 show the resulting dynamic behavior in terms of dimensional and non-dimensional ground-frame lateral position (y) and time (t), as well as already dimensionless heading angle (ψ). Examination of Figure 11 shows a significant difference in heading oscillation frequency in dimensional time that is removed when heading is plotted against non-dimensional time ($\bar{t}$). Furthermore, examination of Figure 12 shows a significant difference in *both* amplitude and the frequency of oscillations in lateral position (y). Both disparities are significantly reduced when the normalized position is plotted against normalized time.

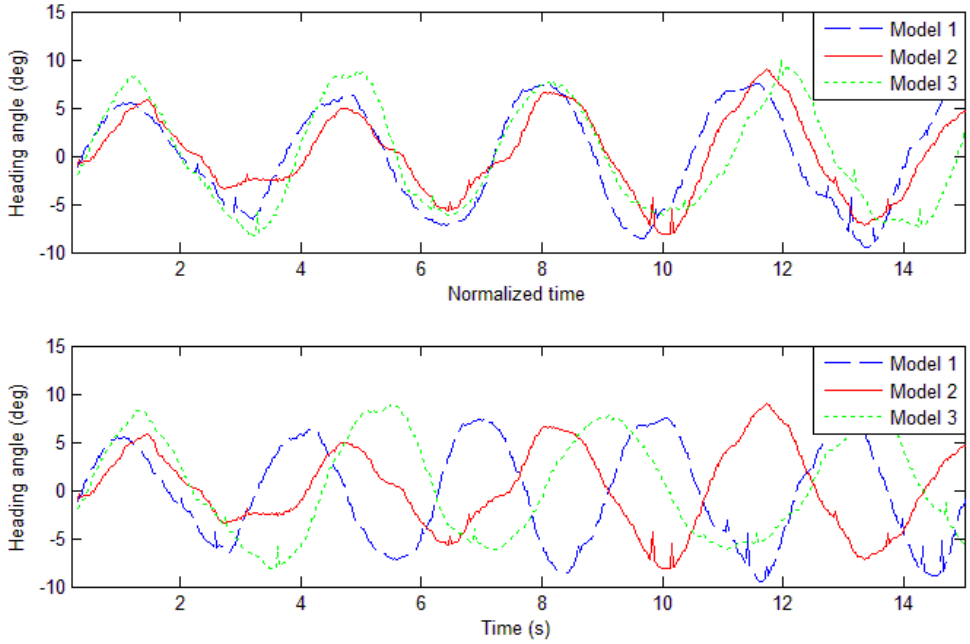

Figure 11: Heading angle response for three different scale models versus normalized and absolute time.

2.4.4 Summary of results

The aforementioned results describe and assess a lab-scale platform for the dynamic characterization of lighter-than-air AWE systems, specifically the Altaeros BAT. A dynamic model-based dimensional analysis suggested that properly-scaled testing parameters will lead to dynamic equivalence across all the lab-scale models. Similar behavioral trends were observed in a set of test results wherein the heading angle response and non-dimensional lateral offset at different scales collapsed onto a single curve.

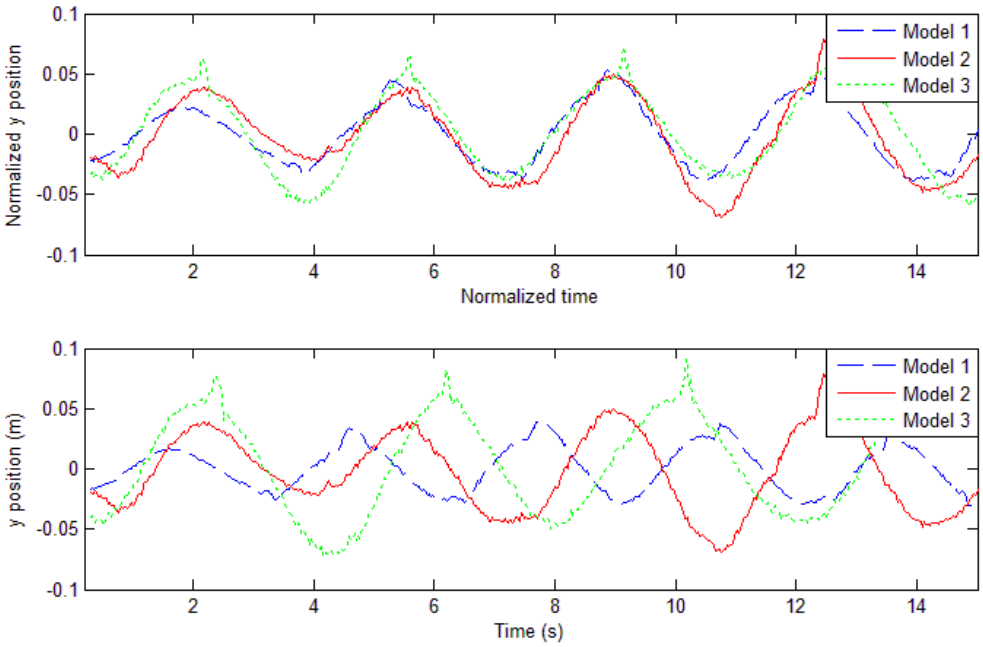

Figure 12: Comparison plot of absolute and normalized lateral position versus normalized and absolute time.

CHAPTER 3: EXPERIMENTALLY INFUSED OPTIMIZATION USING GRADIENT-BASED DOE - MATHEMATICAL FORMULATION

The gradient-based DoE is an iterative optimization process that consists of the following four steps:

- Generate experiments within the *local* parameter space surrounding the estimated optimal design based on the numerical system model.
- Run those experiments.
- Compute a correction to the numerical model based on the experiments.
- Run a full numerical optimization with the corrected model, then repeat the process.

The basic framework in Figure 13 seeks to select optimal values for plant parameters, $\mathbf{p_p}$ and controller parameters, $\mathbf{p_c}$, according to an objective function, $J(\mathbf{p_p}, \mathbf{p_c})$, that accounts for important performance attributes. The specific steps in this framework are as follows:

- A full nested numerical optimization is performed, wherein the controller is optimized fully at every iteration of the plant.
- A local grid-based DoE is performed, in which several variants of the numerically-optimized plant and controller are selected to be tested (in addition to the numerically-optimized plant and controller).

- Selected experiments are run, and the corresponding performance index is quantified in the form of a *cost function* value.

- The cost function estimate is corrected, using experimental results from the recent iteration.

The process of iterating between a set of experiments and a full numerical optimization is repeated until a convergence criterion is reached.

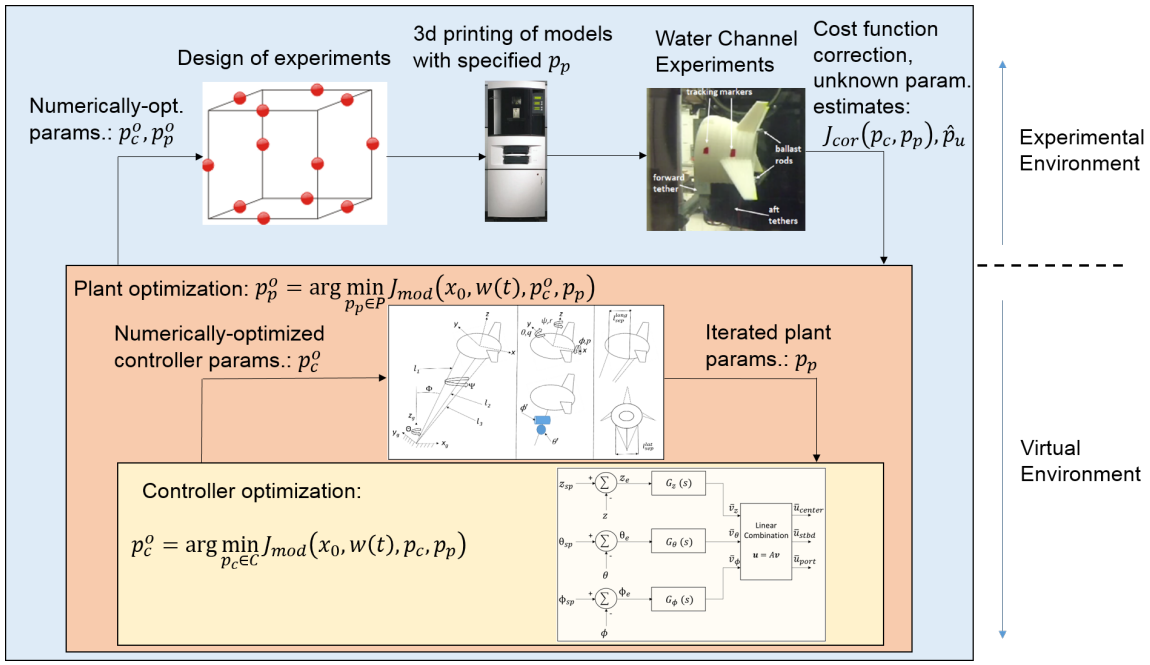

Figure 13: Nested optimization strategy using experimental infusion and numerical model correction.

Before choosing the plant and controller parameters for optimization, open-loop characteristics of the system were studied. Different models with various configurations of the BAT were tested to study the stability and performance characteristics in an open loop environment. Because [33], [34], [35] and all identify *lateral* flight dynamics as the primary challenge to obtaining stable, well-damped flight characteristics, the analysis focused on

the variation of the heading angle and lateral position. Each experiment was conducted under a prescribed flow speed profile and included a controlled lateral perturbation at each flow speed. More precisely, the controlled lateral perturbation consisted of reeling the three tethers sequentially to induce lateral oscillations. Each experiment was characterized using a cost function (J) that considered the lateral dynamics of the system, namely, the heading angle and lateral offset from water channel centerline, as follows:

$$J = \int_{T_i}^{T_f} (K_1 \psi(t)^2 + K_2 y(t)^2)\, dt \tag{20}$$

Here, K_1 and K_2 were chosen to be 0.2 and 0.0125, respectively (where ψ is measured in *rad* and y is measured in m), and $T_i,\ T_f$ denote the start and end time of the test (where $T_f - T_i$ is constant for all the experiments). The weights, K_1 and K_2, were chosen to take under consideration the fact that ψ and y are measured in different physical units and are restricted to different ranges, but are otherwise equally important.

The study presented here compares the impact of the center of mass location (% chord), fin angle of incidence (degrees), and tether attachment configuration (1 forward, 2 aft and 2 forward, 1 aft) on the system performance, as quantified in equation (20). Figure 14 shows the resulting cost function values for different variations in the center of mass location, fin angle of incidence and tether attachment configurations.

For the case study presented in this chapter, the optimization is narrowed down to two very important system parameters, namely the center of mass position, x_{cm} and the trim pitch angle, θ_{sp}, which are shown in Figure 14 to dramatically influence flight performance. To preserve the dynamic equivalence at 1/100-scale, in a water channel environment, p_p was be taken as the *chord-normalized* center of mass location, relative to the center of buoy-

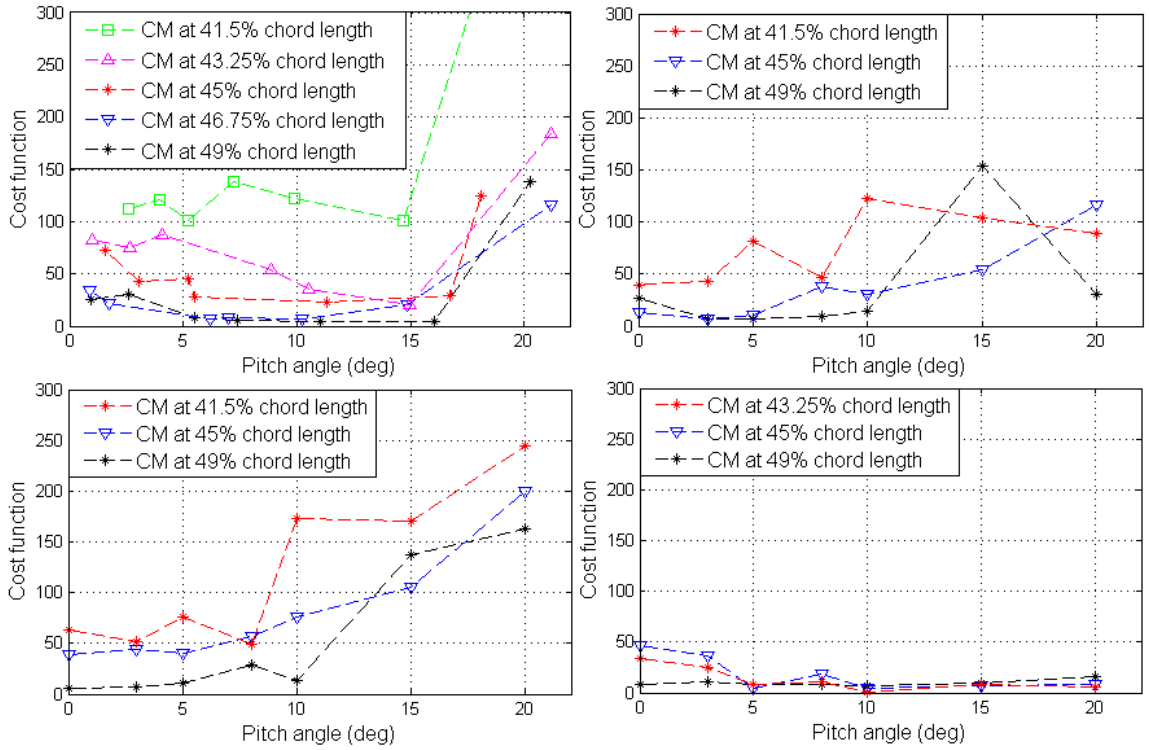

Figure 14: All figures show cost function value versus trim pitch angle and center of mass location for different tether and fin angle configurations. The figure on the top left is for a 0-degree fin angle of incidence and one forward, two aft tether configuration. The figure on the top right is for -5 degree fin angle of incidence. The bottom left figure shows data for +5 degree fin angle of incidence and the last figure is for a 0-degree fin angle with a two forward, one aft tether attachment configuration.

ancy (i.e., $p_p = \frac{x_{cm} - x_{cb}}{x_{chord}}$, where x_{cb} is the center of buoyancy location and x_{chord} is the chord length), whereas p_c is taken as the trim pitch angle, θ_{sp}, which is already dimensionless (radians).

3.1 Performance index

The objective function for experimentally infused optimization was chosen to take under consideration several system properties, including:

- Net energy production;
- Ground footprint, i.e., the horizontal projected area of land that the BAT covers when

swept through its entire swinging circle, which determines land usage requirements and spacing requirements for multiple systems;

- Quality of flight;
- Manufacturing, maintenance, and auxiliary control costs.

Mathematically, the cost function can be denoted by the integral sum of errors in the set point values, control inputs and zenith angle as follows:

$$J = \left[\int_{T_i}^{T_f} (k_1(\psi - \psi_{flow})^2 + k_2\theta_e^2 + k_3\phi_e^2 + k_4 z_e^2 + k_5(\mathbf{u}^T\mathbf{u}) + k_6\Phi)^2 \quad \mathrm{d}t \right] + k_7(x_{cm} - x_{cb})^2(T_f - T_i). \tag{21}$$

Here, $\psi - \psi_{flow}$ denotes the difference between the yaw angle and the direction of water and serves as a measure of both the pointing accuracy of the BAT and its quality of flight. θ_e, ϕ_e, and z_e represent pitch, roll, and altitude tracking errors, respectively. All of these serve as indicators of flight quality. $\mathbf{u}$ is a vector of control inputs, which are linked to energy consumption. Φ is the zenith angle, which is responsible for the ground footprint (where the precise ground footprint is given by $A_{projected} = \pi L_t^2 \sin^2\Phi$). The final cost function term places a direct penalty on ballasting choices that place the center of mass apart from the center of buoyancy. The weights k_1 through k_7 account for a mismatch in the units and ranges for different terms in the objective function.

3.2 Test profile for numerical simulations and experiments

Equally important to the cost function itself is the series of perturbations to the model that occur between T_i and T_f. Each experiment conducted in this work consisted of three different water speeds and three lateral perturbations at regular intervals. The perturbation involves pulling in on the aft port tether for one second and holding it there for two seconds, as shown in Figure 15. This sequence induces a roll and pitch up motion. It also lowers the altitude and results in fluctuations in heading angle until the closed loop control brings the BAT back to the set points. The perturbation profile is shown in Figure 15. For a test run of 300 s, the first 100 s consisted of a relatively slow water speed of 0.205 m/s, followed by 100 s at 0.245 m/s, and 100 s at 0.285 m/s. After every speed change, there is a settling period of 20 s, followed by a controlled lateral perturbation.

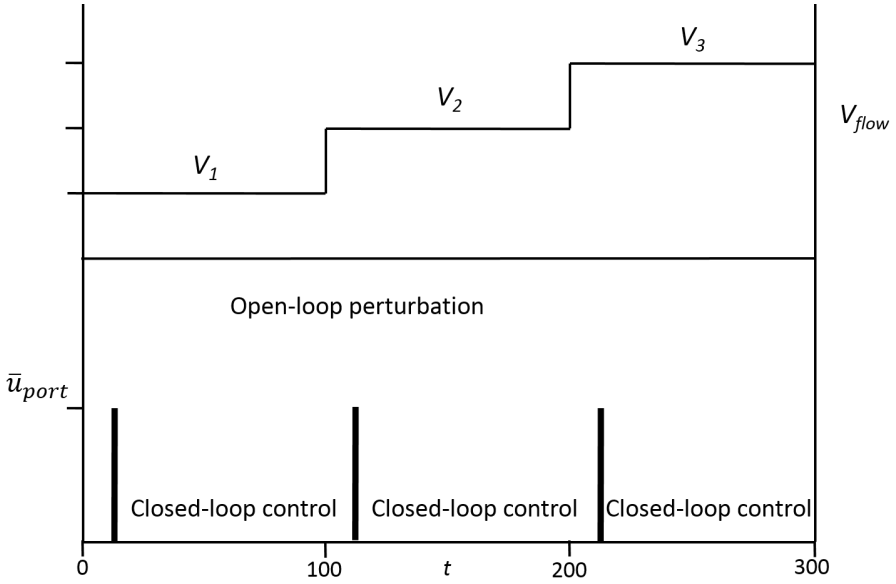

Figure 15: The flow speeds (defining the flow profile) and control inputs (defining the perturbation profile) over the course of one experiment/simulation.

Mathematically, this perturbation is expressed as:

$$\bar{u}_{center} = \begin{cases} 0, & \text{if } t \in T_1 \\ 0, & \text{if } t \in T_2 \\ \bar{v}_z - \bar{v}_\theta, & \text{otherwise} \end{cases} \tag{22}$$

$$\bar{u}_{port} = \begin{cases} -u_{max}, & \text{if } t \in T_1 \\ 0, & \text{if } t \in T_2 \\ \bar{v}_z + \bar{v}_\theta - \bar{v}_\phi, & \text{otherwise} \end{cases} \tag{23}$$

$$\bar{u}_{stbd} = \begin{cases} 0, & \text{if } t \in T_1 \\ 0, & \text{if } t \in T_2 \\ \bar{v}_z + \bar{v}_\theta + \bar{v}_\phi, & \text{otherwise} \end{cases} \tag{24}$$

where the time windows in seconds are given as:

$$T_1 = [20\ 21] \cup [120\ 121] \cup [220\ 221] \tag{25}$$

$$T_2 = (21\ 23] \cup (121\ 123] \cup (221\ 223] \tag{26}$$

3.3 Numerical optimization

First, a full numerical optimization is run, resulting in numerically-optimized plant and controller parameters specified by p_p^* and p_c^*. The cost function used for the numerical optimization, $J_{mod}(p_c, p_p)$, comprises both the base cost function, $J(p_c, p_p)$ and the *correction term*, $J_{cor}(p_c, p_p)$, that was identified from the previous round of experiments, thus yielding $J_{mod}(p_c, p_p) = J(p_c, p_p) + J_{cor}(p_c, p_p)$. This correction term, which is applied at

the second and all of the subsequent iterations, guides the numerical optimization in a direction that it otherwise would not be led. For the specific Altaeros BAT case study, the numerical optimization used a nested approach, wherein a full controller optimization was performed at each iteration of the plant optimization. However, the underlying structure of the numerical optimization is not restrictive in the general case.

3.4 Gradient-based DoE

Following each numerical optimization, it is necessary to determine *which* experiments to run. The optimal selection of experiments for information maximization is presented in the next chapter. For this work, however, a simple grid-based DoE was chosen. This included a total five test runs, which were sufficient to establish an experimental gradient of the cost function with respect to p_c and p_p. Those test runs included the numerically-optimized plant and controller parameters, p_c^*, p_p^*, plus the following set of experiments:

- $p_c = p_c^* + \delta p_c$, $p_p = p_p^*$;
- $p_c = p_c^* - \delta p_c$, $p_p = p_p^*$;
- $p_p = p_p^* + \delta p_p$, $p_c = p_c^*$;
- $p_p = p_p^* - \delta p_p$, $p_c = p_c^*$.

where δp_c and δp_p are fixed-sized variations about the numerically-optimized plant and controller. Because p_p represented the chord-normalized center of mass location for our case study, variations in p_p were accomplished by moving ballast to different ballasting holes in the model. Variations in p_c, the trim pitch angle (θ_{sp}) were accomplished even more easily, simply by entering a different trim value into the GUI on the host computer.

3.5 Experimental correction

After each round of experiments, the experimental results must be digested in a way that provides guidance for the subsequent numerical optimization. This can be done through either of at least two mechanisms (or a combination thereof):

1. Direct parameter identification of a subset of system parameters;

2. Derivation of a cost function correction term, $J_{cor}(p_c, p_p)$, based on experimental results.

Since the uncertainties in this numerical model are the result of unmodeled dynamics, it is not possible or even appropriate to apply correction terms to individual model parameters between experiments. Instead, it is more appropriate to apply the correction directly to the cost function. For the Altaeros BAT case study, that cost function correction term was updated based on the experimentally-identified gradient of the cost as follows:

$$\begin{aligned} J_{cor}(p_c, p_p) &= J_{cor,prev}(p_c, p_p) + R_p \frac{\partial J}{\partial p_p}(p_p^* - p_p) \\ &\quad + R_c \frac{\partial J}{\partial p_c}(p_c^* - p_c), \end{aligned} \tag{27}$$

where $J_{cor,prev}(p_c, p_p)$ is the previous correction term, and R_p and R_c are scalar weighting parameters between 0 and 1 that reflect the level of trust in the experimental gradient calculation. For this case study, $R_p = R_c = 0.1$.

CHAPTER 4: GRADIENT-BASED EXPERIMENTALLY INFUSED DESIGN OPTIMIZATION - EXPERIMENTAL RESULTS

The results of a two-parameter AWE case study are presented here, wherein a total of three iterations of experimentally infused optimization were conducted, using the water channel setup for experiments. The parameters considered in this case study were the longitudinal center of mass location and the trim pitch angle. The objective function to be minimized was given by equation (21).

4.1 Optimization results using two parameters

An initial iteration of numerical optimization resulted in pitch set point of 17.3 degrees and center of mass location at 46.1 % of the total chord length, as measured from the leading edge, with the center of buoyancy at 45.4 % chord. Three iterations of experimentally infused optimization resulted in an optimum pitch set point of 19.4 degrees and the optimum center of mass at 49.3 % of the chord length.

Table 3 shows the results of the optimization, demonstrating that the experimental infusion is effective in driving the optimization toward an improved set of parameters. Figures 16 - 18 show the resulting experimental yaw, roll, and pitch error squared, respectively, illustrating improved performance with the experimental infusion. This work served as an initial step towards experimentally infused optimization and was published in [43].

Table 3: Parameters and cost function values at every iteration.

Iteration	Center of mass location CM_x ((%) of chord)	Pitch set point θ (degrees)	Numerical cost (corrected)	Experimental cost
1	46.1	17.3	4.35	6.85
2	50.1	18.9	4.20	6.12
3	49.3	19.4	4.01	5.81

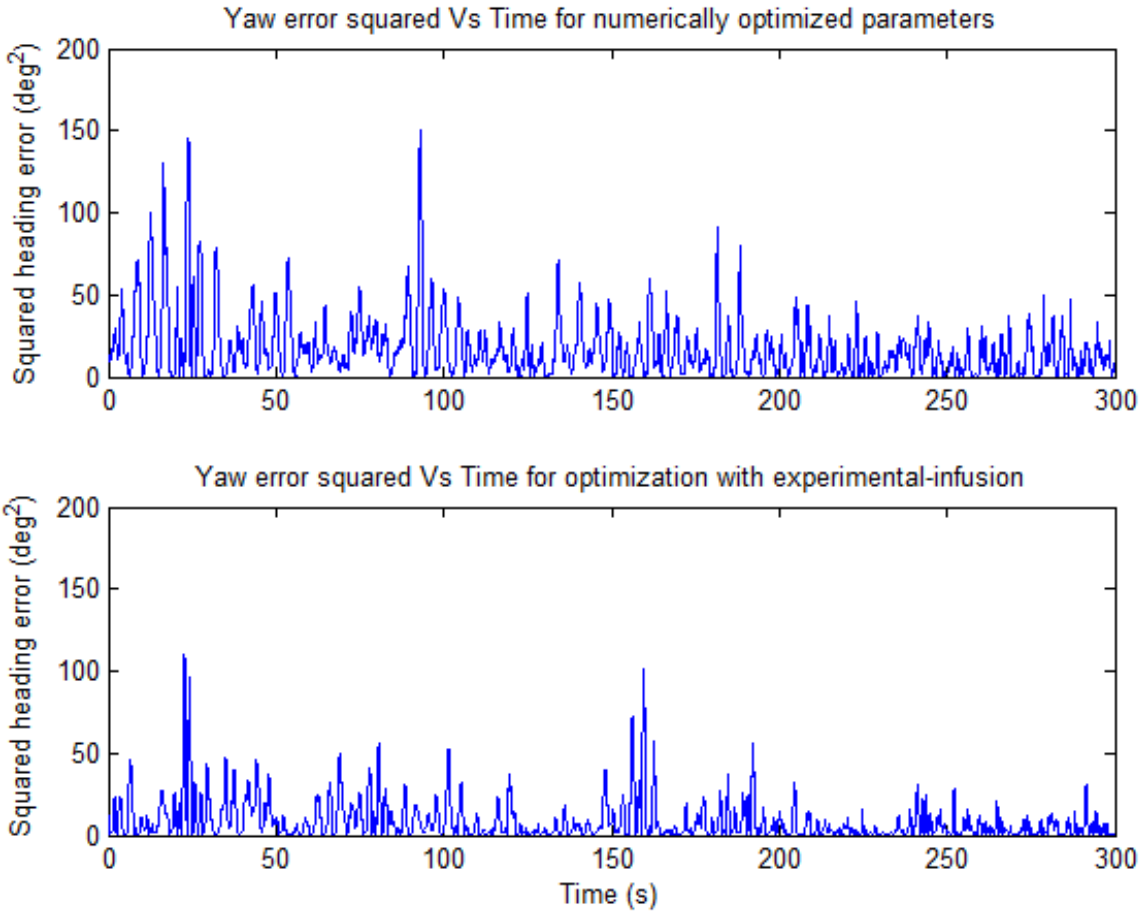

Figure 16: Yaw error squared over the duration of an experiment.

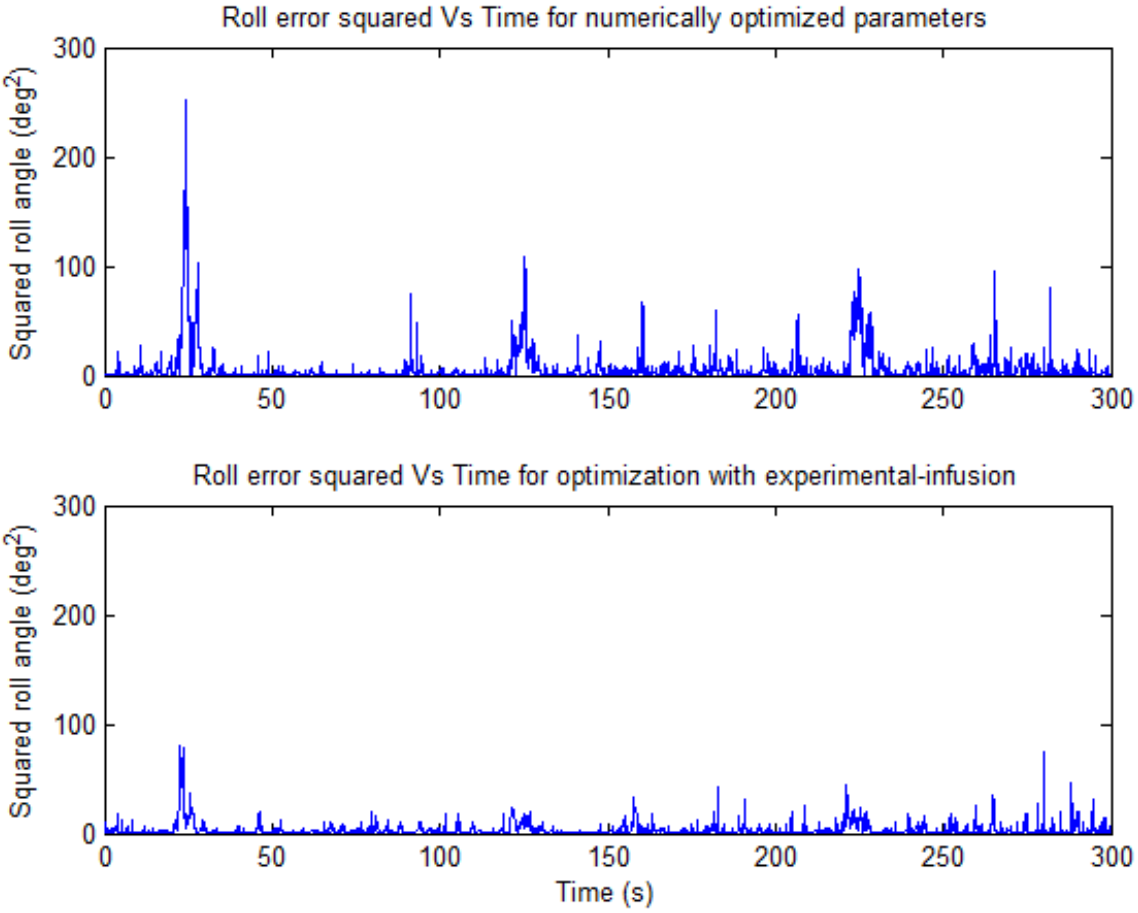

Figure 17: Roll error squared over the duration of an experiment.

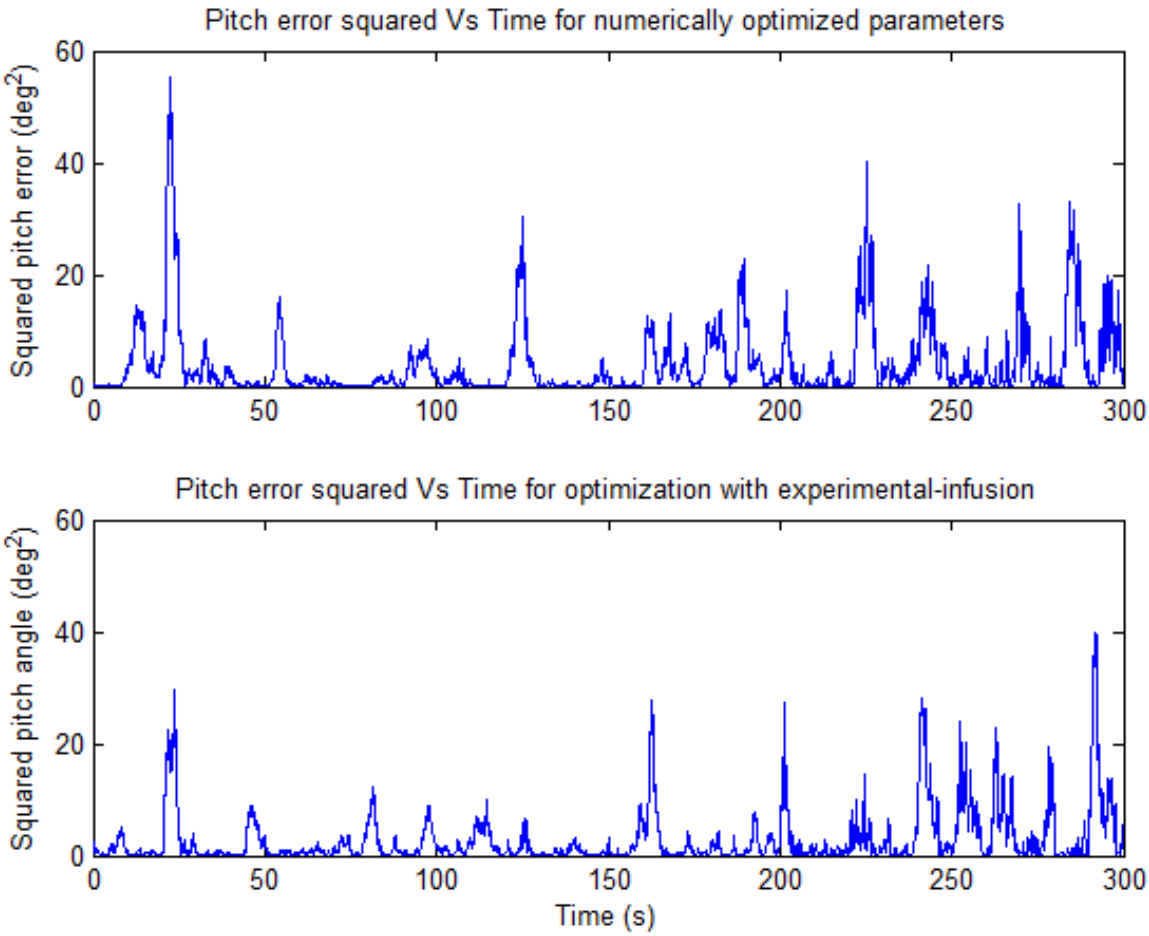

Figure 18: Pitch error squared, showing the pitch angle tracking quality before and after experimentally infused optimization.

CHAPTER 5: OPTIMAL DOE-BASED EXPERIMENTALLY INFUSED DESIGN OPTIMIZATION - MATHEMATICAL FORMULATION

Although the methodology described in the previous chapter yielded promising results, the experiments at each iteration were designed only in the vicinity of the estimated optimal configuration. This local DoE can lead to a situation, particularly with a complex system and many design parameters, where convergence to the globally optimal design is not achieved.

Moreover, with the previous gradient-based DoE, the number of required experiments increases significantly with increasing numbers of design parameters. To address these limitations, a general framework consisting of the following major steps (that are also illustrated in Figure 4 and later clarified with specific details in Figure 19) has been developed:

- Perform an optimal design of experiments (DoE) and numerical simulations that spans a prescribed design space.
- Run the experiments and simulations.
- Fit a response surface to the data obtained from simulations and experiments.
- Improve the numerical model at each iteration based on the results of all previous experiments.
- Reduce the feasible design space for subsequent iterations.

Each of the processes described in Figure 19 is explained in detail as follows:

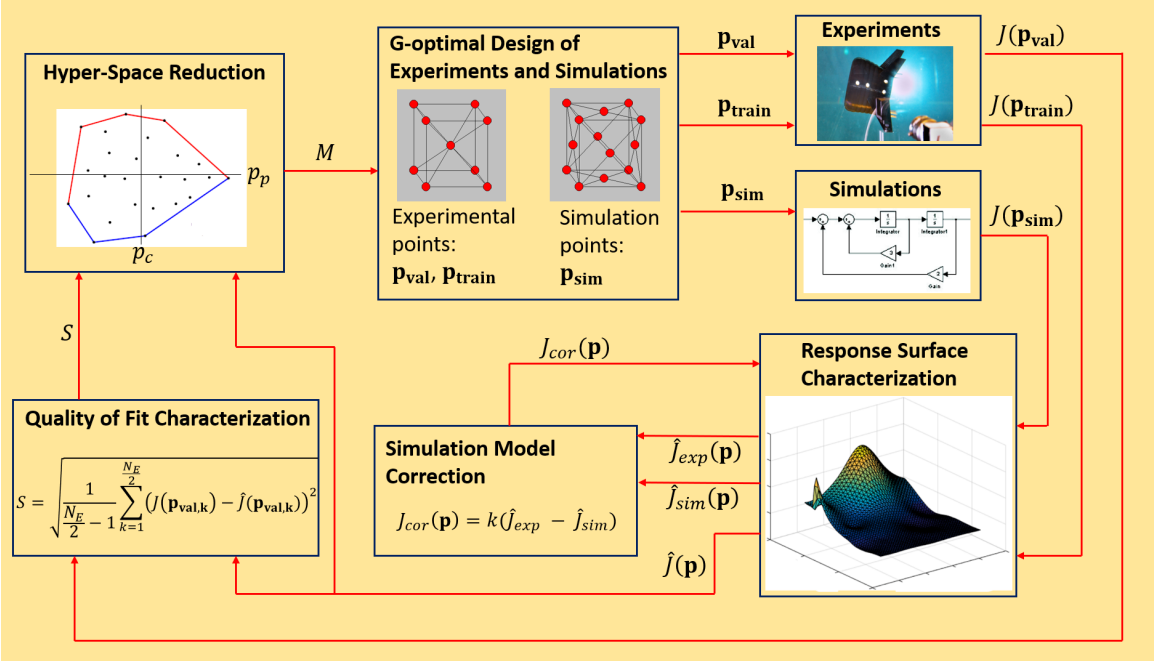

Figure 19: Flowchart demonstrating the sequence of steps involved in the optimal DoE-based optimization. These include: G-optimal DoE in a wide parameter space, followed by experiments, simulations, response surface characterization, model correction, and shrinking of the design space through hypothesis testing ([44] and [45]).

5.1 Optimal DoE

The overarching objective of optimal DoE is to choose experiments within a prescribed design space that maximize information with as few experiments as possible. Such information maximization techniques are used throughout the DoE literature (see [46] and [47]). Unlike the gradient-based experimental design technique used in Chapter 3, optimal DoE techniques select experimental points that maximize properties of the *information matrix*, detailed in [48] and [49]. Some of the widely used optimal DoE techniques include A (average)-optimal, D (determinant)-optimal, G-optimal, E (eigenvalue)-optimal, and T (trace)-optimal design. The D-optimal design is the most popular technique used in the literature. However, the optimality of a D-optimal design is predicated on the assumption that

the exact structure of the model is known. Consequently, D-optimal design often results in numerous repeated experiments, rather than extensive design space exploration. The G-optimality criterion (or global criteria), on the other hand, has been shown to perform well in producing a space-filling design that is significantly informative and does not repeat design points (see [50]). For this case study, because the structure of the system model is unknown and highly speculative, the G-optimality criterion is used in designing two sets of points, namely the numerical simulations and experiments, where N_S simulations and N_E experiments are chosen at each iteration.

G-optimal design relies on the speculation of a m element column vector known as the regressor vector, $r(\mathbf{p_p}, \mathbf{p_c})$, which encodes the anticipated structural dependency of the system output (performance index value in this case) on system parameters. The matrix of n such regressor vectors can be expressed as:

$$R = [r_1 \quad r_2 \quad . \quad . \quad r_n]^T \tag{28}$$

Here, n corresponds to the number of design points (either numerical simulations or experiments). The G-optimality criterion minimizes the maximum prediction variance over the design space, where the optimum design points are given by:

$$[\mathbf{p_p}, \mathbf{p_c}] = arg \min_{(\mathbf{p_p}, \mathbf{p_c}) \in \mathbf{M}} r_i^T (R^T R)^{-1} r_i \tag{29}$$

Here, r_i denotes the regressor vector corresponding to the i^{th} design point. In the AWE application, the chosen regressor vector is quadratic in the plant ($\mathbf{p_p}$) and controller ($\mathbf{p_c}$) parameters. M represents the design space at a given iteration, defined in Figure 19.

At every iteration, the N_E experimental design points are split into an equal number of training and validation points. The experimental points are sorted based on their distance from each other, and alternate points are considered as training and validation points to obtain better coverage of the design space. The training, validation and simulation configurations are denoted by $\mathbf{p_{train}}$, $\mathbf{p_{val}}$ and $\mathbf{p_{sim}}$, respectively.

5.2 Numerical simulations and experiments

Experiments and numerical simulations are conducted for every $\mathbf{p_{train}}$, $\mathbf{p_{val}}$ and $\mathbf{p_{sim}}$, using identical operating conditions. A performance index denoted by $J(\mathbf{p_{train}})$, $J(\mathbf{p_{val}})$ and $J(\mathbf{p_{sim}})$ is computed for training experiments, validation experiments and simulations, respectively.

5.3 Response surface characterization and numerical model correction

Three different response surfaces are characterized at every iteration of the optimization process:

1. A pure experimental response using both training and validation experiments, $\hat{J}_{exp}$;

2. Pure simulation-based response, $\hat{J}_{sim}$;

3. A combined experimental training and simulation-based response, $\hat{J}$;

The G-optimal design points, $\mathbf{p_{train}}$, $\mathbf{p_{val}}$ and $\mathbf{p_{sim}}$, only comprise a discrete set of points in the feasible design space. To compute the optimal design, it is necessary to characterize/estimate the performance index over the entire continuous design space. In order to do this, multiple techniques can be used. Over the course of this research, three techniques have been used and are described as follows:

5.3.1 Regression-based response surface approximation

The combined response surface is estimated using the expression:

$$\hat{J}(\mathbf{p}) = r(\mathbf{p})^T \mathbf{b} \tag{30}$$

Here, $\hat{J}(\mathbf{p})$ is the estimated cost at any point $\mathbf{p}$, and $\mathbf{b}$ is the vector of regression coefficients obtained by minimizing the weighted sum of squared errors given by:

$$\mathbf{b} = arg \min_{\mathbf{b} \in \mathbb{R}^n} \sum_{i=1}^{n} w(\mathbf{p_i})(J(\mathbf{p_i}) - \mathbf{r}_i^T \mathbf{b})^2 \tag{31}$$

Here, $w(\mathbf{p_i})$ is the weight on i^{th} point, which allows for the weighing of training experiments and simulations differently. The idea behind using different weights on experiments versus simulations is to account for different levels of confidence in experiments and simulations.

5.3.2 Distance-weighted response characterization

When the true nature of the response surface cannot easily be described through a simple regressor vector or is unknown entirely, a polynomial approximation may result in poor characterization of the response surface. A distance-weighted approximation, on the other hand, generates more realistic nature of the response surface. In this formulation, the performance associated with any point $\mathbf{p}$ is approximated as the weighted summation of performance indices at all measured points $\mathbf{p_i}$, placing more weight on points that are close to $\mathbf{p}$. The estimated performance under this distance-weighted approximation is given by:

$$\hat{J}(\mathbf{p}) = \frac{\sum_{i=1}^{n} w_i J(\mathbf{p_i})}{\sum_{i=1}^{n} w_i}, \tag{32}$$

$$w_i = \frac{1}{d(\mathbf{p}, \mathbf{p_i})^2} \tag{33}$$

where $d(\mathbf{p}, \mathbf{p_i})$ is the Euclidean distance between $\mathbf{p}$ and $\mathbf{p_i}$.

5.3.3 Squared-exponential response characterization

The third candidate choice for response characterization is a squared exponential fit, which approximates the cost function value at a candidate design point ($\hat{J}(\mathbf{p})$) as a weighted average of measured costs, where the weights are scaled based on normalized distance. The estimated cost function value at a candidate design point $\mathbf{p}$ is given as:

$$\hat{J}(\mathbf{p}) = \frac{\sum_i J(\mathbf{p_i}) e^{(-c(||\mathbf{p}-\mathbf{p_i}||))^2}}{\sum_i e^{(-c(||\mathbf{p}-\mathbf{p_i}||))^2}} \tag{34}$$

where c is a user-defined tuning parameter.

5.4 Numerical model improvement

The experimental results at a given iteration can (and should) be used to improve the numerical model for the next iteration. This is done through a numerical model correction term, $\hat{J}_{cor}(\mathbf{p})$. Once the experimental cost ($\hat{J}_{exp}$) and numerical cost ($\hat{J}_{sim}$) is obtained, the correction term ($\hat{J}_{cor}$) is applied to numerical simulations as follows:

$$\hat{J}_{num,i}(\mathbf{p}) = \hat{J}_{sim,i}(\mathbf{p}) + \hat{J}_{cor,i}(\mathbf{p}) \tag{35}$$

$$\hat{J}_{cor,i}(\mathbf{p}) = k(\hat{J}_{exp,i}(\mathbf{p}) - \hat{J}_{sim,i}(\mathbf{p})) + \sum_{j=1}^{i-1} \hat{J}_{cor,j}(\mathbf{p}) \tag{36}$$

Here, $\hat{J}_{num}(\mathbf{p})$ represents the corrected simulation cost by considering a cumulative correction term $\hat{J}_{cor}(\mathbf{p})$ that consists of a combination of a correction at the current iteration (i) and the cumulative correction over all previous iterations. k is a weight that limits the correction to a certain percentage of the difference between the experimentally-derived and numerical response surface, at every iteration. Hence, as the iterations progress, the nu-

merical cost approaches the experimental cost. The corrected numerical model is used to fit a combined response surface, along with the training experimental data. The estimated optimum parameter combination, $\hat{\mathbf{p}}^*$, is obtained from this combined response, and the corresponding estimated optimal cost is denoted by $\hat{J}(\mathbf{p}^*)$. $\mathbf{p_i}$ corresponds to the batch of design points for the i^{th} iteration, which must be contained within the design space for the i^{th} iteration.

5.5 Feasible design space reduction

The next step in the iterative framework is to shrink the design space by rejecting all candidate configurations that are sufficiently worse than the estimated optimum. This estimated optimum configuration, $\hat{\mathbf{p}}^*$, is the configuration that minimizes the combined response $\hat{J}$. A candidate configuration in the gridded design space is then retained (or rejected) based on the level of confidence that the candidate design is worse than $\hat{\mathbf{p}}^*$. This goal is achieved using hypothesis testing and z-test (see [51]). The null hypothesis (H_0) and alternate (H_1) hypothesis are defined as,

$$H_0 \quad : \quad J(\mathbf{p}) = \hat{J}(\hat{\mathbf{p}}^*) \tag{37}$$

$$H_1 \quad : \quad J(\mathbf{p}) > \hat{J}(\hat{\mathbf{p}}^*) \tag{38}$$

The z test is used to reject a candidate configuration by comparing the corresponding z-score to a threshold z_0 for the desired confidence interval.

$$z(\mathbf{p}) = \frac{\hat{J}(\mathbf{p}) - \hat{J}(\hat{\mathbf{p}}^*)}{S\sqrt{2}} \tag{39}$$

$$S = \sqrt{\frac{\sum_{i=1}^{\frac{N_E}{2}} (\hat{J}(\mathbf{p_{val}}) - J(\mathbf{p_{val}}))^2}{\frac{N_E}{2} - 1}} \tag{40}$$

The term S is referred to as the *quality of fit* between the combined response at validation points and the true experimental response at validation points. A candidate configuration is retained only if the z-score for that configuration is less than the z_0 based on a prescribed confidence interval, taken as 90% for this work.

CHAPTER 6: CONVERGENCE ANALYSIS FOR THE OPTIMIZATION FRAMEWORK

Chapter 4 showed that the framework for experimental infusion with iterative, gradient-based DoE resulted in a system response that was significantly better than the numerically optimized response for the AWE application. Specifically, numerical model improvement allowed for a better estimate of the optimum parameters. The framework was later enhanced in Chapter 5 through the consideration of the global design space at every iteration, along with a cumulative model correction. Therefore, an interesting set of questions one could ask is:

- Under what conditions can one conclude that the corrected numerical model ($\hat{J}_{num}$) will converge to the true system model (J_{true})?
- If precise convergence cannot be guaranteed, can one derive a bound on the closeness with which the model will ultimately converge to the true system response?
- Can such a convergence bound be derived in the presence of some bounded experimental noise?

6.1 Convergence analysis for the numerical model correction

The main focus of convergence analysis is to determine the *closeness* of corrected numerical model response to the true system response in presence of noise and structural uncertainties in the response surface. This is achieved by using a recursive sequence for

the cost function correction, as shown in equation (35). Let J_{sim} be the actual simulation response, and let J_{true} denote the true system response. Let e_1 be the error between actual and estimated response from simulations. Let e_2 be the error between true system and estimated response from experiments. The estimation errors at the n^{th} iteration are expressed as:

$$\begin{aligned} e_{1,n} &= \hat{J}_{sim,n} - J_{sim} \\ e_{2,n} &= \hat{J}_{exp,n} - J_{true} \end{aligned} \tag{41}$$

Assumptions: At every iteration, the estimation errors are assumed to be bounded by a theoretical upper limit, E_n. Hence, the following assumptions are made:

1. $||e_{1,i}|| \leq E_{1,i}$ for $i = 1,2,3,....,n$, and

2. $||e_{2,i}|| \leq E_{2,i}$ for $i = 1,2,3,....,n$

where the function norm, $||.||$, is defined as:

$$||J(\mathbf{p})|| \triangleq \left(\int_M |J(\mathbf{p})|^p \mathrm{d}\mathbf{p} \right)^{\frac{1}{p}} \tag{42}$$

Here, the values of $E_{1,i}$ and $E_{2,i}$ depend on (i) the level of noise present in experiments (in the case of $E_{2,i}$) and (ii) the quality of fit for the response surface. Per (42), the norms of the *functions* $e_{1,i}$ and $e_{2,i}$ are defined based on the concept of an L^p signal norm, but are computed over a multi-dimensional finite design space. The analysis that follows will hold for any finite (positive) integer value of p. Because the size of the design space (M) becomes smaller at each iteration, $E_{1,i}$ and $E_{2,i}$ are monotonically decreasing functions of

the iteration number, and we may define their limits as:

$$E_{1,\infty} = \lim_{i\to\infty} E_{1,i}, \tag{43}$$

$$E_{2,\infty} = \lim_{i\to\infty} E_{2,i}. \tag{44}$$

Let $\hat{J}_{num,n}$ be the corrected numerical model at the n^{th} iteration. The following proposition demonstrates that the numerical response surface converges closely to the true response in the limit, as iterations go to infinity. Furthermore, the asymptotic "closeness" of the corrected numerical model to the true response is dictated by the maximum discrepancy between the response surfaces and the corresponding data used to generate those response surfaces.

Proposition: Under the cumulative correction law of equation (35), $\lim_{n\to\infty} ||\hat{J}_{num,n} - J_{true}|| \leq 2E_{1,\infty} + E_{2,\infty}$.

Proof: Based on the cumulative correction law of equation (35):

$$\begin{aligned} \hat{J}_{num,1} &= \hat{J}_{sim,1} + k(\hat{J}_{exp,1} - \hat{J}_{num,0}) \\ &= \hat{J}_{sim,1} + k(\hat{J}_{exp,1} - \hat{J}_{sim,1}) \end{aligned} \tag{45}$$

$$\begin{aligned} \hat{J}_{num,2} &= \hat{J}_{sim,2} + k(\hat{J}_{exp,1} - \hat{J}_{sim,1}) \\ &+ k(\hat{J}_{exp,2} - \hat{J}_{num,1}) \\ &= \hat{J}_{sim,2} + k(\hat{J}_{exp,1} - \hat{J}_{sim,1}) \\ &+ k(\hat{J}_{exp,2} - \hat{J}_{sim,1} - k(\hat{J}_{exp,1} - \hat{J}_{sim,1})) \\ &= \hat{J}_{sim,2} + k(1-k)(\hat{J}_{exp,1} - \hat{J}_{sim,1}) \\ &+ k(\hat{J}_{exp,2} - \hat{J}_{sim,1}) \end{aligned} \tag{46}$$

The n^{th} term can be written as follows:

$$\begin{aligned}\hat{J}_{num,n} &= \hat{J}_{sim,n} \\ &+ k(\sum_{r=0}^{n-2}(1-k)^r(\hat{J}_{exp,n-r}-\hat{J}_{sim,n-r-1}) \\ &+ (1-k)^{n-1}(\hat{J}_{exp,1}-\hat{J}_{sim,1}))\end{aligned} \tag{47}$$

Therefore, based on the estimation error:

$$\begin{aligned}\hat{J}_{num,n} &= \hat{J}_{sim,n} \\ &+ k(\sum_{r=0}^{n-2}(1-k)^r(J_{true}-J_{sim} \\ &+ e_{2,n-r-1}-e_{1,n-r-1}) \\ &+ (1-k)^{n-1}(J_{true}-J_{sim}+e_{2,1}-e_{1,1}))\end{aligned} \tag{48}$$

Using equation (41), (48) can be modified as follows:

$$\begin{aligned}\hat{J}_{num,n} &= J_{sim}+e_{1,n} \\ &+ k\sum_{r=0}^{n-1}(1-k)^r(J_{true}-J_{sim}) \\ &+ k(\sum_{r=0}^{n-2}(1-k)^r(e_{2,n-r-1}-e_{1,n-r-1}) \\ &+ (1-k)^{n-1}(e_{2,1}-e_{1,1}))\end{aligned} \tag{49}$$

However, the third term to the right hand side of equation (49) reduces to $(1-(1-k)^n)(J_{true}-J_{sim})$. Since $k<1$, $\lim_{n\to\infty}(1-(1-k)^n)=1$. Let $R_n = k(\sum_{r=0}^{n-2}(1-k)^r(e_{2,n-r-1}-e_{1,n-r-1})+(1-k)^{n-1}(e_{2,1}-e_{1,1}))$. Therefore:

$$\lim_{n\to\infty}(\hat{J}_{num,n}-J_{true}) = e_{1,n}+R_n \tag{50}$$

Define an intermediate iteration $\bar{M} \stackrel{\Delta}{=} n - \bar{N}$, where $\bar{N}$ is fixed. It follows that:

$$\begin{aligned} R_n &= k(\sum_{r=0}^{\bar{M}-1}(1-k)^r(e_{2,n-r-1}-e_{1,n-r-1}) \\ &+ \sum_{r=\bar{M}}^{n-2}(1-k)^r(e_{2,n-r-1}-e_{1,n-r-1}) \\ &+ (1-k)^{n-1}(e_{2,1}-e_{1,1})) \end{aligned} \tag{51}$$

As n becomes large, $\bar{M}$ increases as well. Consequently, last two terms in the aforementioned equation vanish as $n \to \infty$. From this observation and the fact that $E_{1,n}$ and $E_{2,n}$ decrease monotonically with respect to i (due to the monotonic decrease in the size of the design space), it follows that:

$$||R_n|| \leq k(E_{1,n-\bar{M}} + E_{2,n-\bar{M}}) \sum_{r=0}^{\bar{M}-1}(1-k)^r \tag{52}$$

$$= (E_{1,n-\bar{M}} + E_{2,n-\bar{M}})(1-(1-k)^{\bar{M}}) \tag{53}$$

which implies that:

$$\lim_{n\to\infty} ||R_n|| \leq E_{1,\infty} + E_{2,\infty} \tag{54}$$

Therefore, from equations (50) and (54):

$$\lim_{n\to\infty} ||\hat{J}_{num,n} - J_{true}|| \leq 2E_{1,\infty} + E_{2,\infty}. \tag{55}$$

Equation (55) gives a theoretical upper bound on the difference between the corrected numerical model and true response after a large number of iterations. It can be inferred that a good quality of fit and low noise threshold will lead to convergence of the corrected numerical model to the true system behavior.

Table 4: Table showing parameters and their range for optimization. A negative sign on CM^x_{CB} indicates that the center of mass lies behind the center of buoyancy.

Parameter	Unit	Minimum	Maximum
CM^x_{CB}	% of chord	-0.25	-5.85
θ_{des}	degrees	0	15
A^H	scale factor	0.8	1.4
A^V	scale factor	0.85	1.85

6.2 Visualization of the convergence result using the AWE case study

A total of four optimization parameters are chosen for the purposes of assessing convergence on the AWE system:

1. longitudinal center of mass location relative to the center of buoyancy (CM^x_{CB}),
2. pitch angle set point (θ_{des}),
3. horizontal stabilizer surface area (A^H), and
4. vertical stabilizer surface area (A^V).

The parameter bounds for the optimization problem are given in Table 4.

The case study results are presented in two parts:

1. 2-parameter optimization to visualize the actual estimated responses;
2. 4-parameter optimization to see the convergence of numerical model to the true response, within guaranteed bounds based on given limits for experimental noise and

structural uncertainty in the response surface models.

To account for the new design parameters (A^H and A^V) explicitly in the system model, the aerodynamic force and moment coefficients have been partitioned between the shroud/fuselage (denoted by F), the horizontal stabilizer(denoted by H), and vertical stabilizer (denoted by V). The reference areas for the shroud and stabilizers are taken to be the respective surface areas. The coefficients in the modified numerical model are given by:

$$C_{D,L,S}(\alpha,\beta) = C^F_{D,L,S}(\alpha,\beta) + C^H_{D,L,S}(\alpha,\beta)\frac{A^H}{A_{ref}} + C^V_{D,L,S}(\alpha,\beta)\frac{A^V}{A_{ref}} \quad (56)$$

$$\begin{aligned} C_{M_x,M_y,M_z}(\alpha,\beta) &= C^F_{M_x,M_y,M_z}(\alpha,\beta) + C^H_{M_x,M_y,M_z}(\alpha,\beta)\frac{A^H l^H}{A_{ref} l_{ref}} \\ &\quad + C^V_{M_x,M_y,M_z}(\alpha,\beta)\frac{A^V l^V}{A_{ref} l_{ref}} \end{aligned} \quad (57)$$

Here, C_D, C_L, and C_S are the drag, lift and side force coefficients, whereas C_{M_x}, C_{M_y} and C_{M_z} are the roll, pitch and yaw moment coefficients. α and β represent the angle of attack and side slip angle, respectively, whereas A_{ref} and l_{ref} are the reference areas and reference lengths, respectively. The superscripts F, H, and V refer to the main body (fuselage/shroud), horizontal stabilizer, and vertical stabilizer, respectively. The values of l^H and l^V were adjusted such that a constant aspect ratio was maintained for any combination of stabilizer surface areas A^H and A^V, respectively.

6.2.1 Numerical alternative to experiments

Prior to moving directly to the presentation of experimental results, we will first visualize the convergence process in the case where experiments are replaced with a higher-fidelity numerical model, termed a surrogate experimental model, whose results are noise

corrupted. This is done for two reasons:

1. Replacement of the experiments with numerical simulations allows us to run many (30 plus) iterations. This large number of iterations could not economically be run with our current experimental setup.

2. By specifying precise bounds on noise and calculating a precise bound on structural response surface uncertainty, we can confirm that the bounds from the previous proposition indeed hold.

The surrogate experimental model incorporated stall effects for the fuselage and the horizontal stabilizer that were omitted from the numerical model. To model these stall effects, the lift coefficients on body and stabilizer were modeled as follows:

$$C_L^F = \begin{cases} C_{L_0}^F + C_{L_\alpha}^F \alpha^F, & \text{if } |\alpha^F| \leq \alpha_{stall}^F \\ C_{L_0}^F + 2C_{L_\alpha}^F \alpha_{stall}^F - C_{L_\alpha}^F \alpha^F, & \text{otherwise} \end{cases} \tag{58}$$

$$C_L^H = \begin{cases} C_{L_0}^H + C_{L_\alpha}^H \alpha^H, & \text{if } |\alpha^H| \leq \alpha_{stall}^H \\ C_{L_0}^H + 2C_{L_\alpha}^H \alpha_{stall}^H - C_{L_\alpha}^H \alpha^H, & \text{otherwise} \end{cases} \tag{59}$$

Here, $C_L^F(\alpha^F)$ and $C_L^H(\alpha^H)$ denote the lift coefficients for shroud and the horizontal stabilizer, respectively, $C_{L_0}^F$ and $C_{L_0}^H$ are the shroud and horizontal stabilizer lift coefficients at zero angles of attack, $C_{L_\alpha}^F$ and $C_{L_\alpha}^H$ represent the linear lift coefficients, α^F and α^H are the angles of attack, and α_{stall}^F and α_{stall}^H are the angles of attack at which the shroud and horizontal stabilizers stall.

6.2.2 Case study results using surrogate model

A total of 33 iterations were performed for every noise threshold selected. In the case of 2-parameter optimization, the parameters considered were CM^{x}_{CB} and θ_{sp}. G-optimal simulations and experiments are shown in Fig. 20. It is evident that the feasible design space is significantly reduced over iterations. A combined numerical/experimental response surface is shown in the right half of Fig. 20. Fig. 21 compares the convergence bound derived in equation (55) for 2 and 4-parameter optimizations using different noise thresholds. The figure also shows that the size of the design space reduces monotonically. Fig. 22 clearly shows an overall improvement in the quality of flight at the final iteration, particularly in terms of the heading angle response. The ground foot-print is slightly reduced as a result of experimental infusion and numerical model correction.

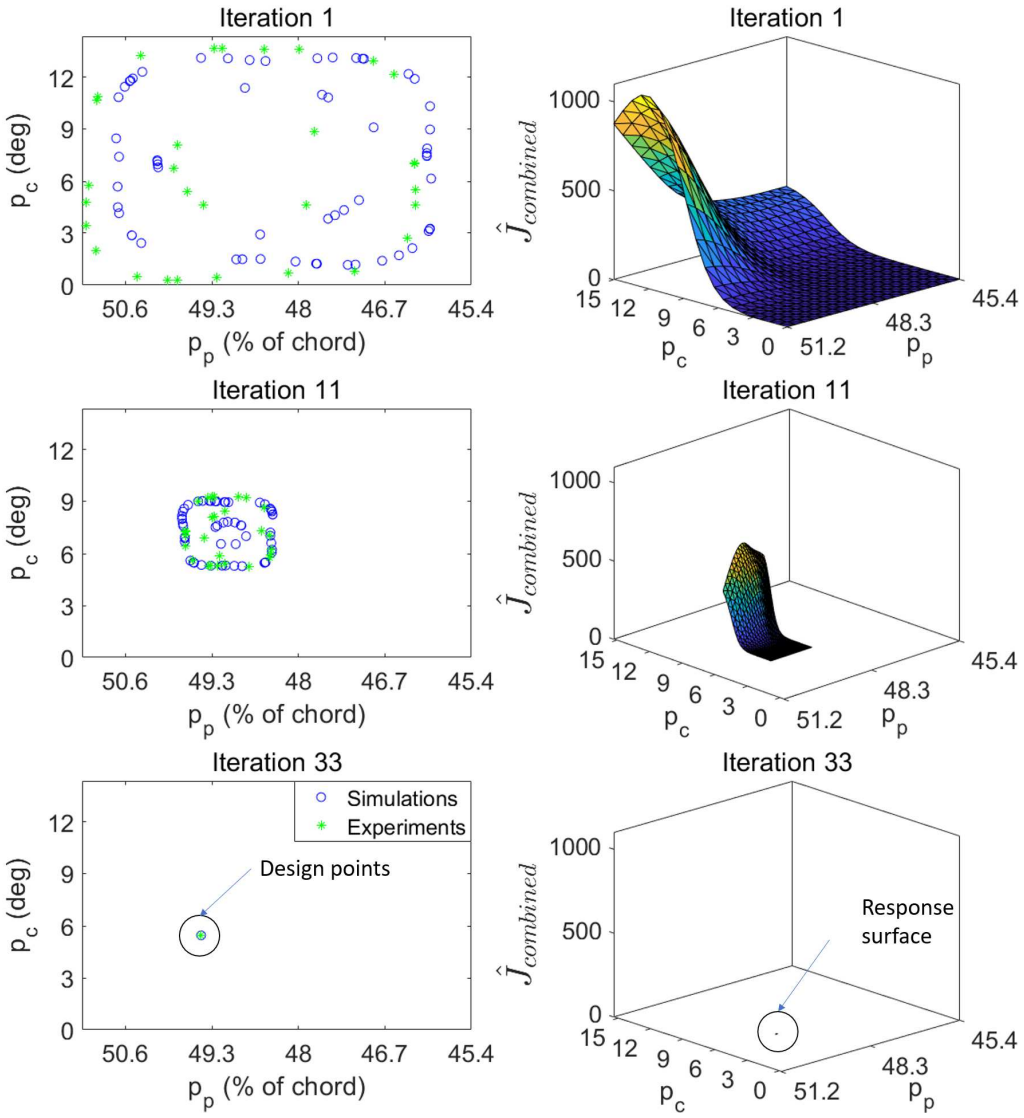

Figure 20: The top row shows design points and combined numerical/experimental response for the very first iteration. The middle row shows the same plots within the reduced design space at an intermediate iteration. The bottom row shows the (dramatically reduced) design space and corresponding response surface at the last iteration.

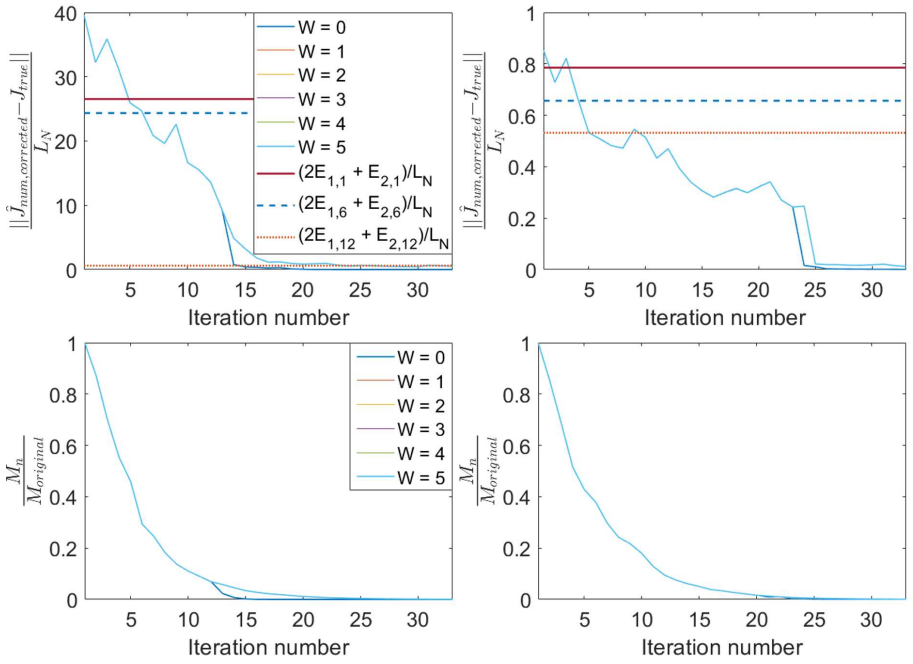

Figure 21: Evolution of $||\hat{J}_{num,n} - J_{true}||$ for 2-parameter (top left) and 4-parameter (top right) optimization. The bottom left and right plots show the evolution of the design space as a fraction of the original design space for 2 and 4-parameter optimization, respectively.

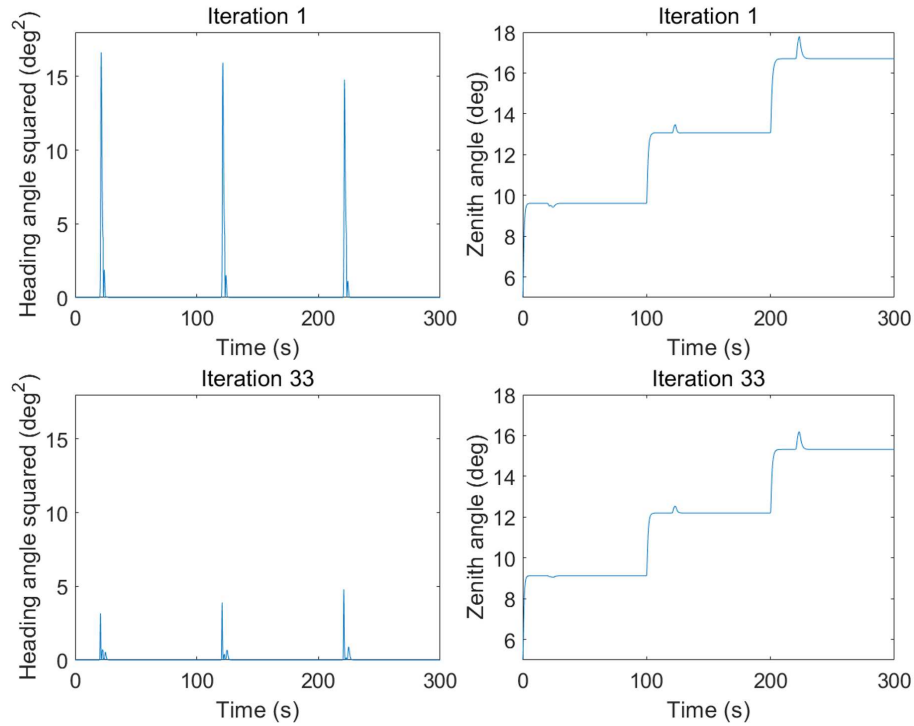

Figure 22: Heading angle comparison between the optimum design at the first and last iterations, which shows significant improvement, whereas, zenith angle plots on right show slight improvement.

CHAPTER 7: OPTIMAL DOE-BASED EXPERIMENTALLY INFUSED DESIGN OPTIMIZATION - EXPERIMENTAL RESULTS

This chapter presents the results of optimal DoE-based experimentally infused design optimization for both a two-and four-parameter case study, using the lab-scale water channel platform for experiments. The cost function was taken to be as follows:

$$J = \int_{T_i}^{T_f} (k_1(\psi - \psi_{flow})^2 + k_2\theta_e^2 + k_3\phi_e^2 + k_4 z_e^2 + k_5(\mathbf{u}^T\mathbf{u}) + k_6\Phi)^2 \quad \mathrm{d}t \tag{60}$$

7.1 Case study results for 2-parameter optimization

In the case of the two-parameter optimization, the framework in Section 5 was used to optimize the longitudinal center of mass location, x_cm (that corresponds to the plant parameter, p_p), and trim pitch angle, θ_{sp} (which corresponds to the control parameter, p_c). The weights, $w(\mathbf{p})$, given by Equation (31) were chosen as follows: training experiments $w(\mathbf{p_{train}})$ had a weight of 80% as compared to only 20% for numerical simulations $w(\mathbf{p_{sim}})$ in the response surface characterization. The regressor vector used in this case was quadratic in plant and controller parameters and is given as:

$$r = [1 \quad p_p^2 \quad p_p \quad p_c^2 \quad p_c]^T \tag{61}$$

The first three iterations of the optimization process are summarized in Table 5, along with the optimal configuration given by pure numerical simulations. Figure 23 shows the experiments and numerical simulations generated at each iteration and the combined response

Table 5: Estimated optimal parameters (values of $\mathbf{p}^*$) at each iteration, with $zero^{th}$ iteration corresponding to pure numerical optimum.

Iteration	x_{cm} (% of chord length)	θ_{sp} (degrees)	Area of feasible design space (% of original design space)
0	45.7	8.29	100
1	49.40	7.21	61.53
2	49.53	5.45	16.52
3	49.53	7.51	15.33

surface characterization. It is evident from the table as well as the figures that design space is shrinking at every iteration, up to the third iteration. Thereafter, the variation in experiments is dictated predominantly by the noise in the experimental data. Hence, further reduction in the design space is limited. The shrinking at the very first iteration is not as significant as that at the second iteration since the numerical model remains uncorrected during the first iteration. At the onset of the second iteration, the numerical model is corrected using experiments, which leads to a better quality of fit between combined numerical plus training data and the validation data. Figure 24 shows that there is a significant improvement in the quality of flight governed by pitch angle tracking and the heading angle throughout the experiment. These results were presented in [52].

7.2 Case study validation through 4-parameter optimization

In the case of the four-parameter optimization, the design parameters were longitudinal center of mass location relative to the center of buoyancy (CM^x_{CB}), trim pitch angle (θ_{sp}), horizontal stabilizer area (A^H), and vertical stabilizer area (A^V).

7.2.1 Modified CAD models with removable fin geometry

Considering large numbers of design parameters requires large numbers of simulations and experiments, demanding a large degree of reconfigurability in the 3D printed models. This reconfigurability allows the experimental operator to rapidly switch between design parameters. The previous 3D printed BAT models have ballast holes and multiple tether attachment points for rapid re-reconfigurability. In addition to the tether attachment points and center of mass locations, vertical and horizontal stabilizers also impact the flight performance, as seen through experimental results in Figure 14 and simulations in Chapter 6. However, with previous 3D printed models, altering either the angle of incidence, dihedral angle or stabilizer areas required the 3D printing of a whole new model. However, 3D printing a new model for every candidate stabilizer geometry is a costly and time-consuming precess when the goal is to run several batches of experiments. To that extent, a new design has been developed for rapid iteration between different sizes of horizontal and vertical stabilizers.

7.2.2 Design characteristics

The new design separates horizontal and vertical stabilizers from the shroud. A set of peripheral T-slots along the shroud are provided for the stabilizers to slide into and out of. To allow smooth sliding of the stabilizers between the T-slots and to hold the stabilizers in place, a clearance of 0.1 mm is provided. The design can achieve a suitable range of center of mass locations while maintaining prescribed excess buoyancy. Moreover, the design is water-tight to maintain known mass distribution and precise center of mass location. This was achieved through an improved stereolithography apparatus (SLA) based 3D-printing

process.

7.2.3 Water-proof 3D printed model with stereolithography apparatus (SLA)

Previous models used in generating the results of Chapter 4 were printed using Fused Deposition Modeling (FDM). FDM slices the geometry to be printed into different layers. The resin is melted and deposited layer by layer to generate the complete part. The FDM process is unable to replicate intricacies in the model and results in a porous part. Unlike FDM, SLA printing deploys photo-polymerization to stack 3D layers of the resin, thereby resulting in a solid fill. Since an SLA printed part has stronger chemical bonding between the layers while connecting the photopolymers, the SLA process is a better choice for this application, which requires a highly consistent and water tight part. Specifically, the Form 2 by Formlabs ([53]) is used to print the part. The Form 2 is equipped with a resin tank at the bottom. The stacked layers on top are separated from the resin tank using side peel process, and a wiper is used to remove the debris, if any. The printer has reasonably fast cure times and great precision. A layer thickness as low as 25 microns can be achieved using this SLA printer. The rate at which this part can be printed on Form 2 using a standard resin is about 15 mm of height per hour. To drain all of the filling material trapped in the hollow cavity, it is recommended to have three holes of 3.5 mm diameter at the bottom of each model. These holes are later plugged to seal the model.

Although a solid fill guarantees water tightness, significant material is shelled out to maintain the net buoyancy, hence resulting in an internal void. The fins. however, are solid and maintain a constant aspect ratio across different surface area designs. For this case study validation, the allowable range for horizontal and vertical fin areas was discretized

Table 6: Table showing estimated optimal parameters (values of $\mathbf{p}^*$) at each iteration. Iteration zero indicates optimum parameters obtained from pure numerical simulations. Negative values for CM^x_{CB} indicates that the center of mass must lie behind the center of buoyancy.

Iteration	CM^x_{CB} (% of chord length)	θ_{sp} (degrees)	A^H (scale factor)	A^V (scale factor)	Hyper volume of feasible design space (% of original design space)
0	-1.16	6.14	0.8	1.77	100
1	-5.62	13.73	1.26	0.88	81.82
2	-5.24	9.76	0.81	1.63	59.87
3	-5.11	9.78	0.84	1.55	32.17
4	-5.09	10.57	0.84	1.44	24.03
5	-5.09	11.61	0.88	1.41	19.57

into 24 steps with equal increments.

7.2.4 Results using water channel experimental setup

The optimization framework of Section 5 has been applied to the lab-scale AWE setup described in Section 2 to optimize four parameters. A total of 18 experiments and 36 simulations were chosen. For this case study, $w(\mathbf{p_{train}})$ and $w(\mathbf{p_{num}})$ are chosen to be 0.7 and 0.3, respectively. Hypothesis testing is performed using a 90 percent confidence interval.

Table 6 shows the optimum parameters and resulting cost for the first five iterations of the experimentally infused optimization. Iteration zero denotes the optimum configuration given by the numerical model. The design space is reduced significantly across these five iterations, as seen from last column in Table 6. Fig. 26 and Fig. 27 show different system

responses for both the numerical and the experimentally-infused optimum. Specifically, the heading angle response is significantly improved through the experimental-infusion. For the numerical optimum, the heading angle response shows spikes over the last 30 seconds. These result from a pair of dots leaving the region of interest for the camera momentarily. However, due to a dynamically updated image processing algorithm, precise tracking of heading angle is regained as the dots re-enter this region of interest. The roll offset is greatly reduced in the case of the experimentally infused optimum, as seen from Fig. 27. This figure also shows that the experimentally infused optimum yields a slightly lower zenith angle. Fig. 28 shows qualitative improvement in the altitude and pitch tracking. Some of these results are documented in [52].

7.3 Conclusions and final remarks

A formal iterative method for combined plant and controller optimization, fusing both simulations and experiments, was proposed in this research. The framework was validated using an AWE application, initially using the center of mass location and pitch angle set-point as optimization variables. A rigorous convergence analysis derived the theoretical limit on numerical model improvement, which was visualized using a surrogate model in place of experiments. Finally, the framework was applied to 4-parameter optimization. Through experimentally infused optimization and a unique lab-scale setup for the experiments themselves, we obtained much better system performance than with the numerical model alone.

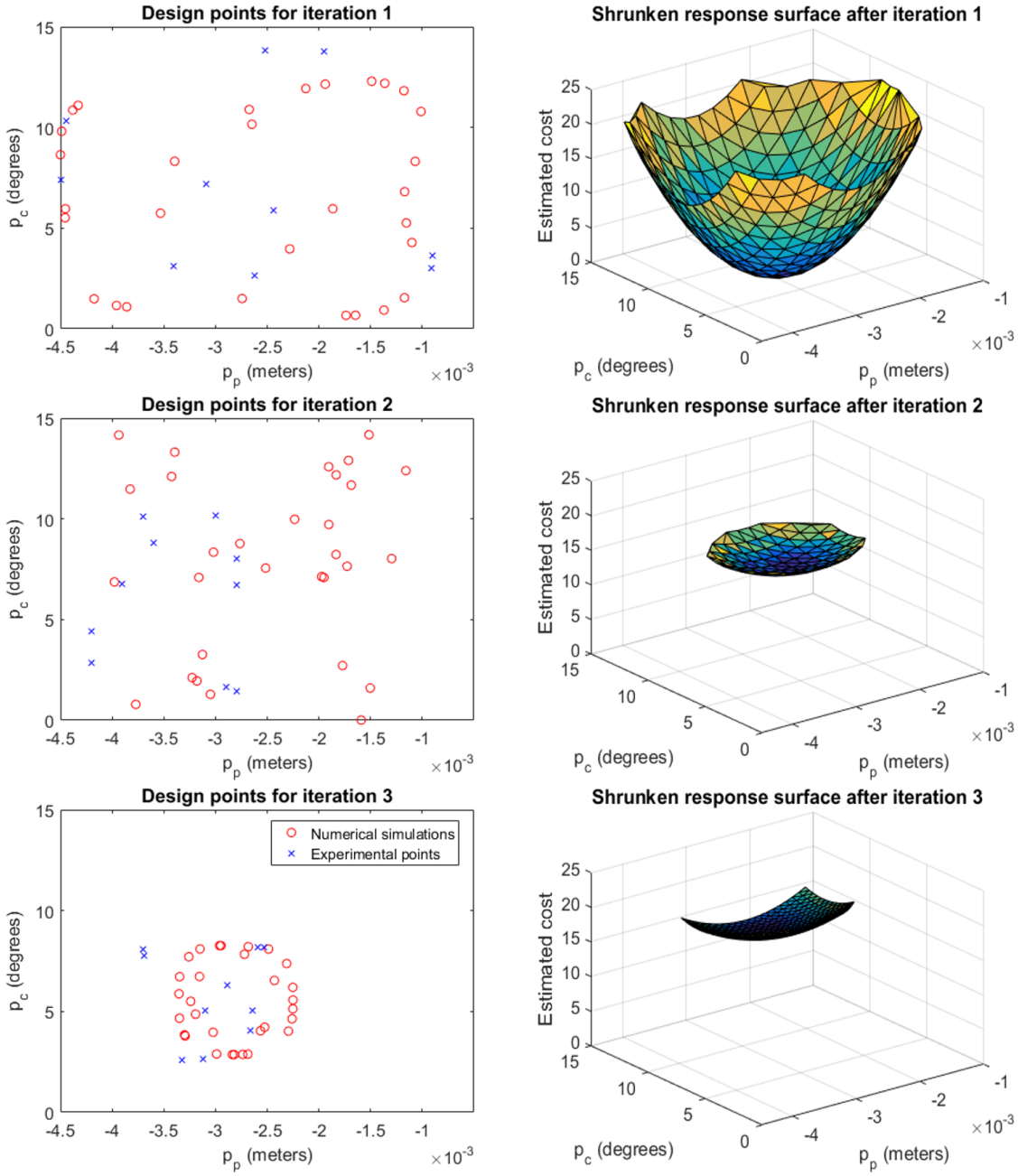

Figure 23: The left half shows experiments and numerical simulations generated by G-optimal design at every iteration in the shrunken design space. The right half shows plots of combined numerical and experimental response surface ($\hat{J}$) for every candidate point (p_p,p_c) in the shrunken design space.

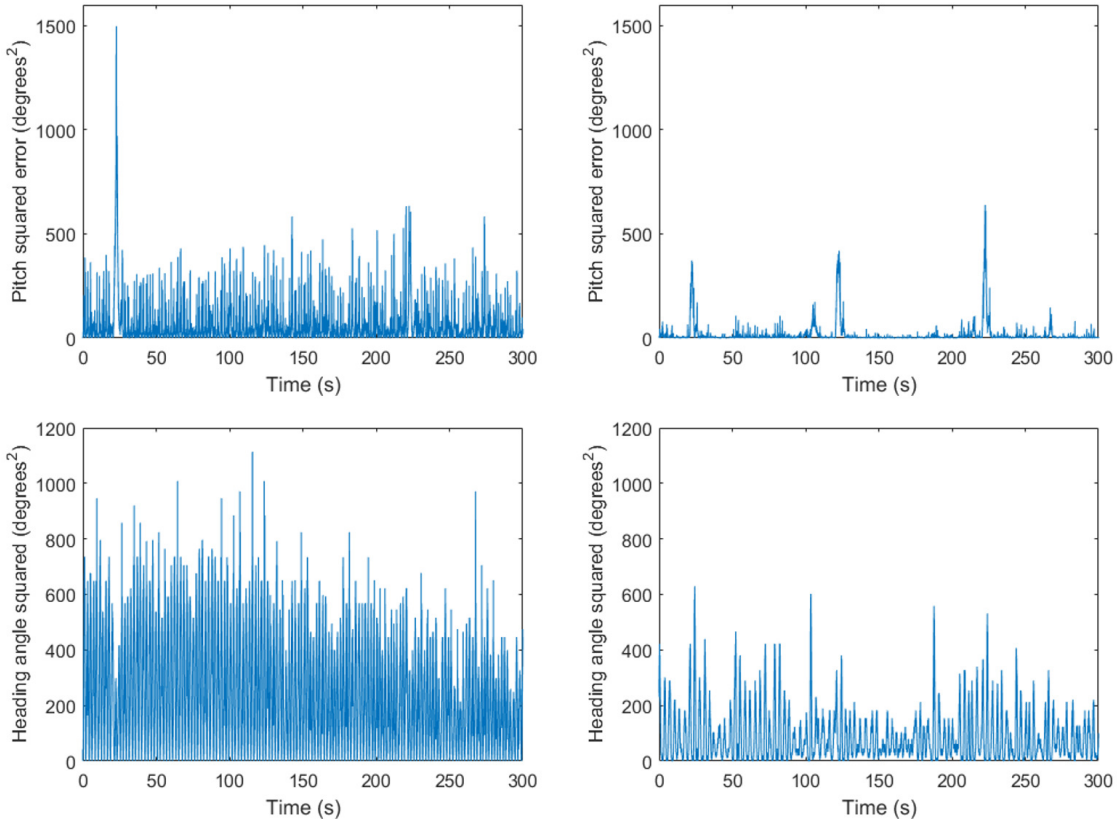

Figure 24: The left and right halves of this figure show a comparison between the numerically optimal configuration and the experimentally infused optimum. The improvement in pitch and heading squared error responses with experimental infusion is evident from the plots.

Figure 25: 3D printed representation of the BAT showing removable fin design, enabling rapid reconfiguration of plant geometry.

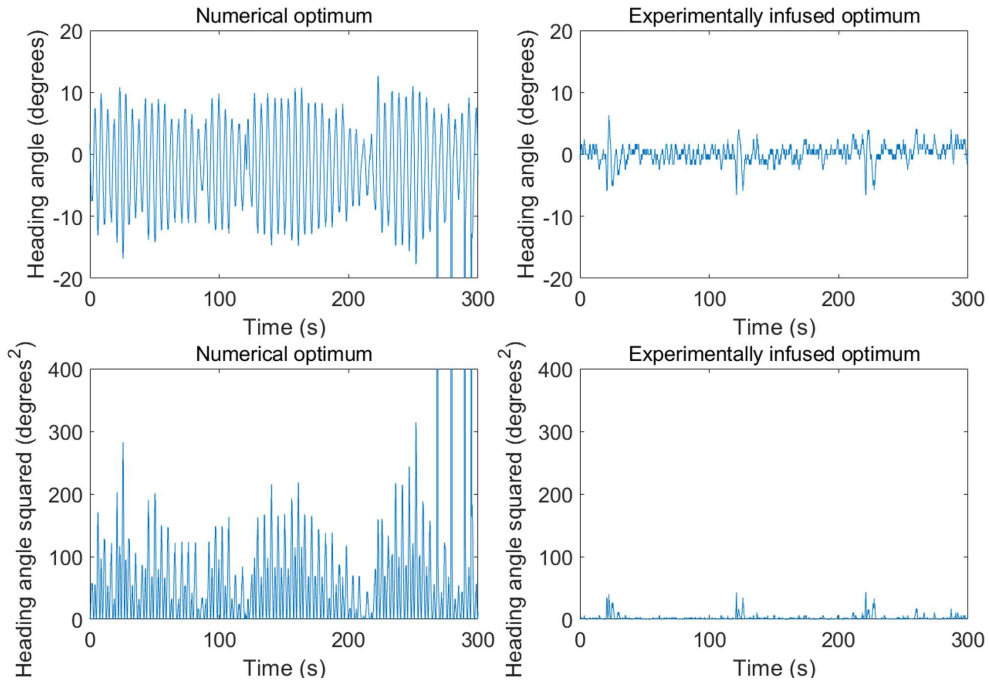

Figure 26: The top row shows a comparison between heading angle for the numerically optimal configuration and experimentally-infused optimum. The bottom row shows a similar comparison between the squared heading angle.

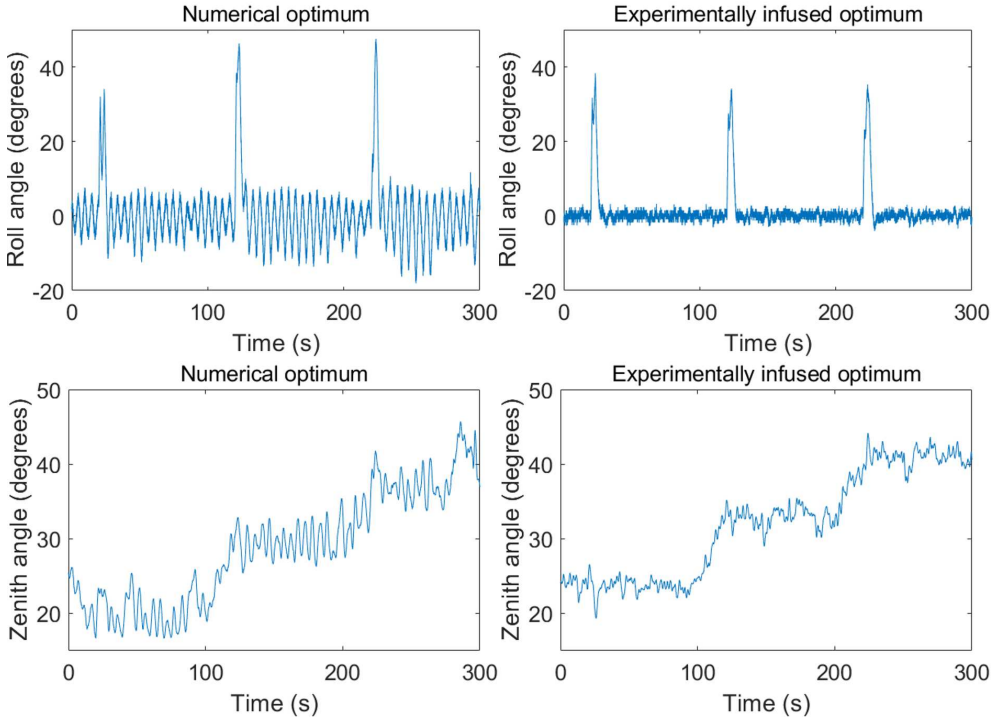

Figure 27: This figure shows a comparison between roll and zenith angle responses for the numerically-optimized design (left) versus the design resulting from the experimentally-infused optimization approach (right).

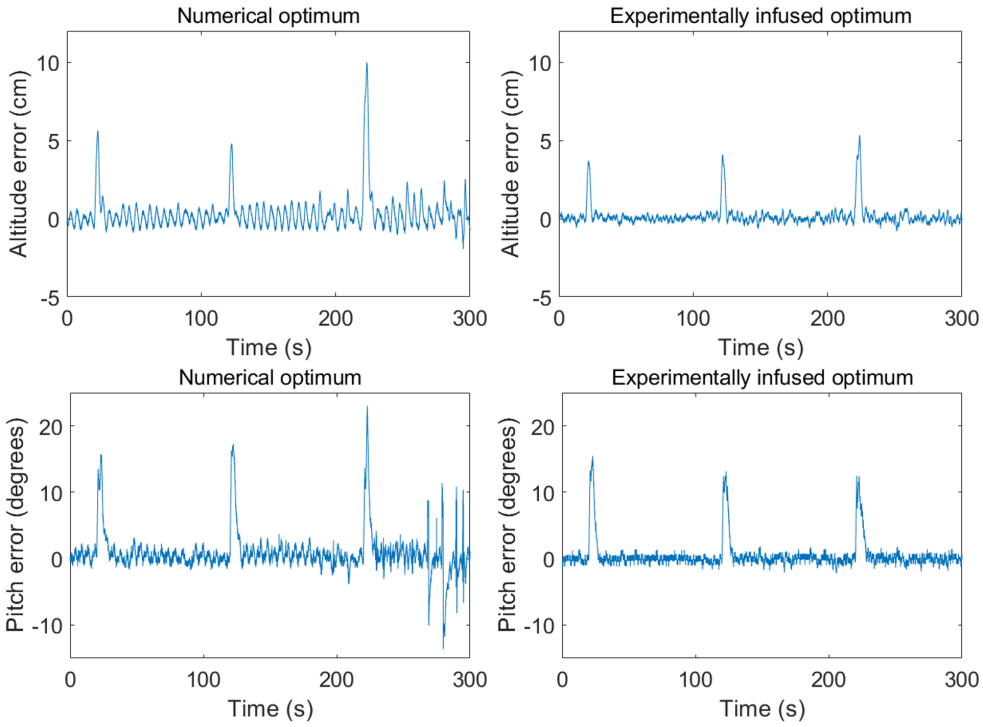

Figure 28: A similar comparison in the altitude and pitch tracking errors implies improved quality of flight through experimental infusion.

REFERENCES

[1] H. K. Fathy, J. A. Reyer, P. Y. Papalambros, and A. G. Ulsoy. On the coupling between the plant and controller optimization problems. In *American Control Conference*, Arlington, VA, 2001.

[2] A. Albert and J. Ottnad. Integrated structural and controller optimization in dynamic mechatronic systems. *Journal of Mechanical Design*, 132(4):041008–8, 2010.

[3] L. R. Carley, G. Ganger, D. F. Guillou, and D. Nagle. System design considerations for mems-actuated magnetic-probe-based mass storage. *IEEE Transactions on Magnetics*, 37(2):657–662, 2001.

[4] T. Ravichandrana, D. Wang, and G. Hepplerb. Simultaneous plant-controller design optimization of a two-link planar manipulator. *Mechatronics*, 16(3-4):233–242, 2006.

[5] Y. Zhu, J. Qiu, and J. Tani. Simultaneous optimization of a two-link flexible robot arm. *Journal of Robotic Systems*, 18(1):29–38, 2001.

[6] S. F. Alyaqout, P. Y. Papalambros, and G. A. Ulsoy. *Combined Design and Robust Control of a Vehicle Passive/Active Suspension*. Proceedings of the European Control Conference. Greece, 2007.

[7] S. F. Alyaqout, P. Y. Papalambros, and G. A. Ulsoy. Combined design and robust control of a vehicle passive/active suspension. *International Journal of Vehicle Design*, 59(4):315–30, 2012.

[8] H. Fathy. Combined plant and control optimization: Theory, strategies and applications. *PhD Dissertation, University of Michigan, Ann Arbor*, 2003.

[9] J. A. Reyer. Combined embodiment design and control optimization: Effects of cross -disciplinary coupling. *PhD Dissertation, University of Michigan, Ann Arbor*, 2000.

[10] M. J. Alexander, J. T. Allison, and P. Y. Papalambros. Decomposition-based design optimization of electric vehicle powertrains using proper orthogonal decomposition. *International Journal of Powertrains*, 1(1):72–92, 2012.

[11] J. T. Allison and S. Nazari. Combined plant and controller design using decomposition-based design optimization and the minimum principle. In *Proceedings of the ASME International Design Engineering Technical Conferences & Computers and Information in Engineering Conference*, Montreal, Quebec, Canada, 2010.

[12] J. T. Allison, T. Guo, and Z. Han. Co-design of an active suspension using simultaneous dynamic optimization. *Journal of Mechanical Design*, 136(8):81003 (14 pages), 2014.

[13] D. L. Peters, P. Y. Papalambros, and A. G. Ulsoy. Sequential co-design of an artifact and its controller via control proxy functions. *Journal of Mechatronics*, 23(4):409–418, 2013.

[14] D. L. Peters, P. Y. Papalambros, and A. G. Ulsoy. Control proxy functions for sequential design and control optimization. *ASME Journal of Mechanical Design*, 133(9):091007 (11 pages), 2011.

[15] D. Peters. Coupling and controllability in optimal design and control. *PhD Dissertation, University of Michigan, Ann Arbor*, 2010.

[16] H. K. Fathy, P. Y. Papalambros, A. G. Ulsoy, and D. Hrovat. Nested plant/controller optimization with application to combined passive/active automotive suspensions. In *American Control Conference*, Denver, CO, 2003.

[17] H. K. Fathy, P. Y. Papalambros, and A. G. Ulsoy. Integrated plant, observer, and controller optimization with application to combined passive/active automotive suspensions. In *ASME International Mechanical Engineering Congress and Exposition, Dynamic Systems and Control*, volume 1, Washington, DC, 2003.

[18] H. Fathy, S. Bortoff, S. Copeland, P. Papalambros, and A. Ulsoy. Nested optimization of an elevator and its gain-scheduled lqg controller. In *ASME International Mechanical Engineering Congress and Exposition*, New Orleans, LA, 2002.

[19] A. C. Pil and H. H. Asada. Integrated structure/control design of mechatronic systems using a recursive experimental optimization method. *IEEE/ASME Mechatronics*, 1(3):191–203, 1996.

[20] Q. Li, W. Zhang, and L. Chen. Design for control-a concurrent engineering approach for mechatronic systems design. *IEEE/ASME Transactions On Mechatronics*, 6(2):161–169, 2001.

[21] M. Moradi, M. Naraghi, and A. Kamali. Simultaneous design of parameters and controller of robotic manipulators: closed loop approach to practical implementation. *Advanced Robotics*, 32(3):105–121, 2018.

[22] C. Archer, L. Monache, and D. Rife. Airborne wind energy: Optimal locations and variability. *International journal of Renewable Energy*, 64:180–186, 2014.

[23] Altaeros energies website, http://www.altaerosenergies.com/.

[24] Ampyx power website, https://www.ampyxpower.com/.

[25] Google makani website, https://x.company/makani/.

[26] Enerkite website, http://www.enerkite.de/technologie.

[27] Kitegen website, http://www.kitegen.com/en/about-2/.

[28] Windlift website, http://windlift.com/.

[29] L. Fagiano, M. Milanese, and D. Piga. Optimization of airborne wind energy generators. *International journal of robust and nonlinear control*, 22:2055–2055, 2012.

[30] P. NikpoorParizi, N. Deodhar, and C. Vermillion. Combined plant and controller performance analysis and optimization for an energy-harvesting tethered wing. In *American Control Conference*, Boston, MA, 2016.

[31] P. NikpoorParizi, N. Deodhar, and C. Vermillion. Modeling, control design, and combined plant/controller optimization for an energy-harvesting tethered wing. *IEEE Transactions on Control Systems Technology*, 26(4):1157–1169, 2018.

[32] J. Deese, N. Deodhar, and C. Vermillion. Nested plant/controller co-design using g-optimal design and extremum seeking: Theoretical framework and application to an airborne wind energy system. In *IFAC World Congress*, volume 50, pages 11965–11971, Toulouse, France, 2017.

[33] C. Vermillion, B. Glass, and B. Szalai. Development and full-scale experimental validation of a rapid prototyping environment for plant and control design of airborne wind energy systems. In *ASME Dynamic Systems and Control Conference*, San Antonio, TX, 2014.

[34] C. Vermillion, T. Grunnagle, R. Lim, and I. Kolmanovsky. Model-based plant design and hierarchical control of a prototype lighter-than-air wind energy system, with experimental flight test results. *IEEE Control Systems Technology*, 22(2):531–542, 2014.

[35] C. Vermillion, B. Glass, and S. Greenwood. Evaluation of a water channel-based platform for characterizing aerostat flight dynamics: A case study on a lighter-than-air wind energy system. In *AIAA Lighter-Than-Air Systems Conference*, Atlanta, GA, 2014.

[36] J. Deese, T. Muyimbwa, C. Deodhar, N. amd Vermillion, and P. Tkacik. Lab-scale characterization of a lighter-than-air wind energy system - closing the loop. In *AIAA Lighter-Than-Air Systems Conference*, Dallas, TX, 2015.

[37] M. Cobb, C. Vermillion, and H. Fathy. Lab-scale experimental crosswind flight control system prototyping for an airborne wind energy system. In *ASME Dynamic Systems and Control Conference*, Minneapolis, MN, 2016.

[38] C. Lambert, A. Saunders, C. Crawford, and M. Nahon. Design of a one-third scale multi-tethered aerostat system for precise positioning of a radio telescope receiver. *CASI Flight Mechanics and Operations Symposium*, 2003.

[39] C. Lambert. Dynamics and control of a multi-tethered aerostat positioning system. *PhD Dissertation, McGill University, Montreal, QC*, 2006.

[40] S. Smoot. Conceptual design and passive stability of tethered platforms. *PhD Dissertation, Stanford University*, 2012.

[41] S. Smoot and I. Kroo. Dimensional analysis and scaling for tethered lifting bodies. In *11th AIAA Aviation Technology, Integration, and Operations (ATIO) Conference*, Virginia Beach, VA, 2011.

[42] N. Deodhar, A . Bafandeh, J. Deese, B. Smith, T. Muyimbwa, C. Vermillion, and P. Tkacik. Laboratory-scale flight characterization of a multitethered aerostat for wind energy generation. *AIAA Journal*, 55(6):1823–1832, 2017.

[43] N. Deodhar, C. Vermillion, and P. Tkacik. A case study in experimentally-infused plant and controller optimization for airborne wind energy systems. In *American Control Conference*, Chicago, IL, 2015.

[44] N. Deodhar and C. Vermillion. A framework for fused experimental/numerical plant and control system optimization using iterative g-optimal design of experiments. In *Proceedings of the ASME International Design Engineering Technical Conferences & Computers and Information in Engineering Conference*, Charlotte, NC, 2016.

[45] N. Deodhar and C. Vermillion. Experimentally-infused active system optimization framework: Theoretical convergence analysis and airborne wind energy case study. *Proceedings of the ASME International Design Engineering Technical Conferences & Computers and Information in Engineering Conference*, 2018.

[46] D. C. Montgomery. *Design and Analysis of Experiments*. John Wiley and Sons Inc, 8 edition, 2012.

[47] R. Jin, W. Chen, and A. Sudjianto. An efficient algorithm for constructing optimal design of computer experiments. In *ASME Design Engineering Technical Conferences and Computers and Information in Engineering Conference*, Chicago, IL, 2003.

[48] J. Liu and M. Shah. Learning human actions via information maximization. In *IEEE Conference on Computer Vision and Pattern Recognition*, Anchorage, AK, 2008.

[49] A. J. Bell and T. J. Sejnowski. An information-maximisation approach to blind separation and blind deconvolution. *Journal of Neural Computation*, 7(6):1129 – 1159, 1995.

[50] W. J. Welch. Computer-aided design of experiments for response estimation. *Technometrics*, 26(3):217–224, 1984.

[51] M. Friedman. The use of ranks to avoid the assumption of normality implicit in the analysis of variance. *Journal of the American Statistical Association*, 32(200):675–701, 1937.

[52] N. Deodhar, J. Deese, and C. Vermillion. Experimentally infused plant and controller optimization using iterative design of experimentstheoretical framework and airborne wind energy case study. *Journal of Dynamic Systems, Measurement, and Control*, 140(1):10, 2017.

[53] Formlabs website: https://formlabs.com/3d-printers/form-2/.